Long-range inhibitory axons from medial entorhinal cortex target lateral entorhinal neurons projecting to the hippocampus

Eirik S. Nilssen Bente Jacobsen Thanh P. Doan
Paulo J. B. Girão Menno P. Witter‡

Kavli Institute for Systems Neuroscience and Centre for Neural Computation, Norwegian University of Science and Technology (NTNU), Trondheim, Norway

ABSTRACT

Functionally distinct information encoded by the two main divisions of the entorhinal cortex (EC), the lateral EC (LEC) and the medial EC (MEC), is thought to be first integrated at the level of the hippocampus. Here we examine a circuit connecting MEC to LEC that supports functional interplay at the level of the two entorhinal domains. Using a combination of anatomical, *in vitro* electrophysiological and behavioral experiments in the mouse, we report that axons from MEC somatostatin-expressing GABAergic neurons densely distribute in layer I of LEC, where they drive strong and near selective inhibition of principal neurons in layer IIa. This inhibitory pathway is accompanied by MEC glutamatergic axons that innervate multiple layers of LEC and preferentially synapse onto principal neurons in layers IIb and III. Our findings indicate that excitatory and inhibitory projections from MEC may separately regulate the activity of different populations of hippocampal-projecting principal neurons in LEC.

‡ Correspondence: menno.witter@ntnu.no

INTRODUCTION

In the mammalian brain, the hippocampus and the parahippocampal region form a system that supports spatial navigation and episodic memory. A critical component of this system is the entorhinal cortex (EC), which provides most of the cortical input to the hippocampus. It is well-accepted that the rodent EC has two main subdivisions commonly referred to as the lateral EC (LEC) and the medial EC (MEC) (Nilssen et al., 2019). These entorhinal areas have different functions and are thus believed to play complementary roles relevant to the formation of episodic memories (Sugar and Moser, 2019). There is strong evidence that MEC represents space through a manifold of functionally specialized neurons, such as grid cells (Fyhn et al., 2004; Hafting et al., 2005; Yartsev et al., 2011; Jacobs et al., 2013), object-vector cells (Høydal et al., 2019), border cells (Savelli et al., 2008; Solstad et al., 2008), speed cells (Kropff et al., 2015; Ye et al., 2018) and head-direction cells (Sargolini et al., 2006; Giocomo et al., 2014), whose collective activity is thought to map self-location as the animal navigates in space. In contrast, spatial coding is much less robust in LEC when animals explore open field environments (Hargreaves et al., 2005; Yoganarasimha et al., 2011), and LEC is believed to instead primarily encode the content, e.g. object and odour-related information (Deshmukh and Knierim, 2011; Xu and Wilson, 2012; Tsao et al., 2013; Igarashi et al., 2014; Wang et al., 2018), as well as temporal sequences of ongoing experiences (Tsao et al., 2018; Bellmund et al., 2019; Montchal et al., 2019; Bright et al., 2020).

The functional dissociation between MEC and LEC indicates that LEC, a neural center for episodic time, could operate independently from MEC, a neural center for space. If so, lateral entorhinal output to the hippocampus is computed without access to information generated by ongoing activity in MEC. Anatomical tracing results, however, speak against a functional isolation of the two entorhinal areas by showing that axons of entorhinal neurons ramify extensively throughout the entire EC, thereby creating a direct line of communication between MEC and LEC. These associational axons mediate communication in both directions across the entorhinal border, but the pathway from MEC to LEC is reportedly more extensive than the reverse pathway from LEC to MEC. In particular, neurons in layer II and V-VI of MEC densely innervate the superficial layers (I–III) of LEC (Köhler, 1986; Swanson and Köhler, 1986; Witter et al., 1986; Köhler, 1988; Dolorfo and Amaral, 1998; Biella et al., 2002b; Chrobak and Amaral, 2007; Ohara et al., 2019). These

observations imply a more substantial information flow in the direction from MEC to LEC than in the reverse direction, and further show that medial entorhinal axons preferentially innervate the layers that supply the main lateral entorhinal input to the hippocampus. In the pathway from LEC to the hippocampus, dentate gyrus (DG), CA2 and CA3 receive synaptic inputs from reelin-expressing principal neurons in layer IIa, whereas CA1 and subiculum are targeted by principal neurons in layer III as well as some calbindin-expressing neurons in layer IIb (van Groen et al., 2003; Kitamura et al., 2014; Kohara et al., 2014; Ohara et al., 2019).

The functional relevance of MEC input to LEC is currently not well understood. Although the signature spatial cells characteristic of MEC are absent in LEC, the latter area has been shown to exhibit task-relevant processing of spatial information, often tied to the introduction of objects in the environment (Keene et al., 2016; Rodo et al., 2017). For example, some neurons in LEC develop spatially confined firing fields signalling the present or past location of objects (Deshmukh and Knierim, 2011; Tsao et al., 2013). Because the two entorhinal subdivisions express widely different connectivity patterns with cortical and subcortical areas (Kerr et al., 2007), it is unclear how LEC has access to spatial information. One possibility is that spatial selectivity in LEC could be inherited from MEC, though the role played by MEC in modulating computations in LEC is yet to be established.

In this study, we used *in vitro* electrophysiology, in combination with neuroanatomical tracing and behavioral experiments, to investigate the associative network connecting MEC to LEC, with a focus on neurons in LEC providing synaptic input to the hippocampus. We find that this pathway is composed of excitatory and long-distance projecting inhibitory axons, and further present evidence that optogenetic activation of these projections has neuron-specific impact in superficial layers of LEC. Activation of somatostatin-expressing (SST^+) GABAergic axons from MEC almost exclusively inhibit principal neurons in layer IIa (PNIIA), whereas input from glutamatergic axons preferentially excites principal neurons in layers IIb (PNIIB) and III (PNIII). Our data provide insight into the organizing principles ruling the MEC–LEC circuit and indicate a role for MEC in exerting selective control over the activity of hippocampal-projecting neurons in LEC.

RESULTS

Glutamatergic neurons and somatostatin-expressing GABAergic neurons in MEC send axons to LEC

We first aimed to identify MEC neurons that send axons to LEC. Retrograde neuroanatomical tracing was conducted in GAD67^{eGFP} mice, which provide genetic access to GABAergic neurons (Tamamaki et al., 2003), to distinguish between glutamatergic and potential GABAergic contributions to this pathway. After injecting either the chemical tracer fluorogold (FG, n = 2 mice) or an adeno-associated virus (AAV2-CAG-tdTomato, n = 1 mouse) into dorsal LEC, tagged neurons in MEC were found in both deep and superficial layers (deep, V-VI; superficial, I-III; 3758 FG/tdTomato^{+} neurons counted from 3 GAD67^{eGFP} mice; Figs. 1A and 1B). Out of a total of 5190 counted FG/tdTomato^{+} neurons in MEC (n = 3 mice), 3.7 ± 2.4% (mean ± s.d) expressed the GFP-signal of GAD67-positive neurons. Since many corticocortical long-distance projecting GABAergic neurons, i.e., GABAergic neurons whose axons project outside of their anatomical area of origin, synthesize the neuropeptide somatostatin (Melzer and Monyer, 2020), we examined if SST^{+} neurons are found among the GABAergic neurons projecting from MEC to LEC. Immunostaining of the tissue revealed that 64.7 ± 22.6% (mean ± s.d) of retrogradely labelled GABAergic neurons were immunoreactive for SST (Figs. 1C and 1D).

To investigate medial entorhinal innervation patterns in LEC, we independently labelled SST^{+} neurons and glutamatergic neurons by injecting a mixture of two viruses into MEC of transgenic SST^{Cre} mice (n = 3). The virus solution had an equal ratio of i) an AAV vector driving GFP expression in glutamatergic neurons under the CamKII promoter (AAV1-CamKII-eGFP-WPRE-rBG) and ii) a Cre-dependent AAV vector encoding tdTomato (AAV1-CAG-FLEX-tdTomato). CamKII-promoted expression led to extensive local green fluorescence, accompanied by axonal labelling in the hippocampus and in LEC. The Cre-driven red fluorescence of SST^{+} neurons was distributed across layers of MEC, with an additional clear labelling in ipsilateral LEC. Within LEC, SST^{+} axons densely innervated layers I and IIa, with some scattered axons in layers IIb and III. Strong viral labelling of glutamatergic axons was found in layers I, IIb and III, with additional weaker axonal labelling in layers IIa and V-VI (Figs. 1E and 1F). In contrast to the dense innervation of LEC by medial entorhinal SST^{+} axons, only very few tagged axons were observed in MEC

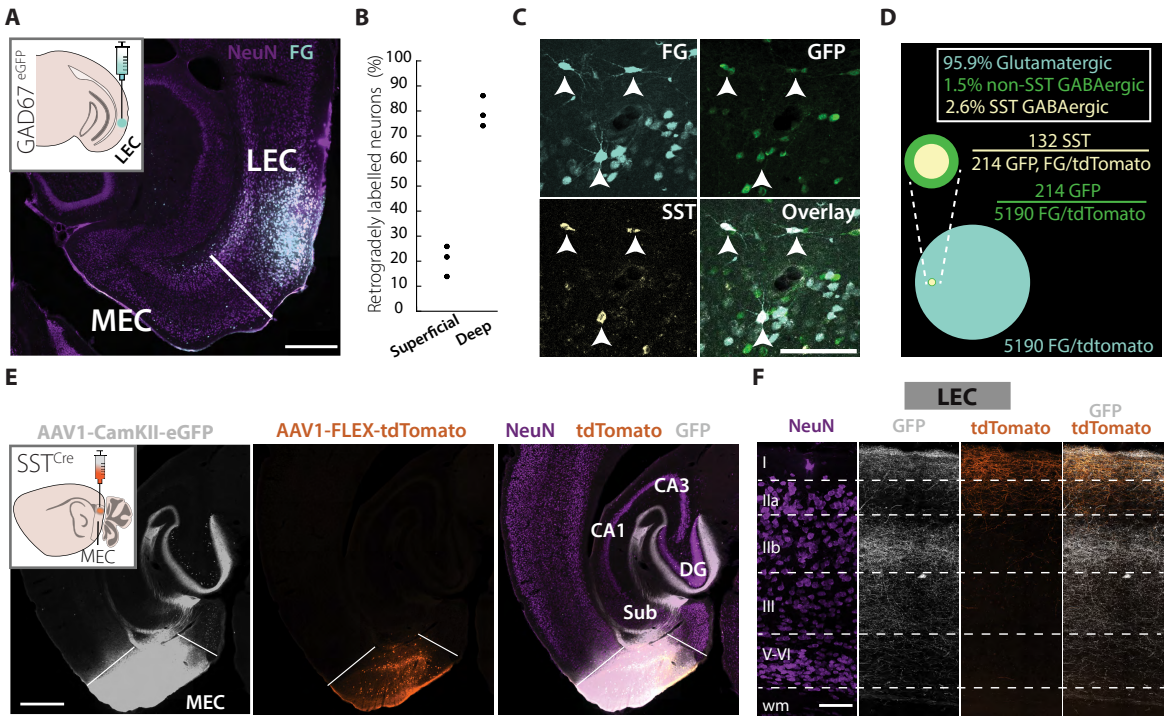

Figure 1. Glutamatergic neurons and SST⁺ GABAergic neurons project from MEC to LEC
(A) Horizontal brain section from a GAD67^{eGFP} mouse showing an FG injection site (light cyan) in LEC. Inset: Schematic of the retrograde tracing experiment. Scale bar, 500 µm. **(B)** Quantification of retrogradely labelled neurons in deep (V–VI) and superficial (I–III) layers of MEC (n = 3 mice). **(C)** SST⁺ GABAergic neurons in MEC project to LEC. Arrowheads indicate examples of triple-labelled neurons (SST⁺, GAD67^{eGFP}, FG) from the experiment in **A**. Scale bar, 100 µm. **(D)** Proportions of GABAergic neurons (SST⁺ and non-SST⁺) and glutamatergic neurons in the MEC-LEC pathway (neuron counts from 3 mice). **(E)** Delivery of an equal mix of AAV1-CAG-FLEX-tdTomato and AAV1-CamKII-eGFP-WPRE-rBG into MEC of SST^{Cre} mice (upper left schematic) selectively labels SST⁺ neurons with tdTomato and glutamatergic neurons with GFP. Sub, subiculum. Scale bar, 500 µm. **(F)** Different laminar innervation patterns in LEC of glutamatergic axons and SST⁺ axons from the experiment in **E**. Wm, white matter. Scale bar, 100 µm.

when targeting the LEC SST⁺ neuron population by injecting AAV1-CAG-FLEX-tdTomato into LEC (n = 2 SST^{Cre} mice; Supplementary Fig. 1). Furthermore, we did not observe any labelled axons innervating LEC following conditional viral tagging of medial entorhinal parvalbumin-expressing (PV⁺) neurons or vasoactive intestinal peptide-expressing (VIP⁺) neurons in PV^{Cre} (n = 5) or VIP^{Cre} (n = 3) mice, respectively (Supplementary Fig. 2). Thus, our data support an exclusivity of SST⁺ neurons as the source of the inhibitory pathway from MEC to LEC, and further show that this inhibitory neuron class does not participate substantially in the reverse pathway that connects LEC to MEC.

To gain insight into the wider circuit that indirectly connects to LEC through the inhibitory MEC–LEC pathway, we mapped brain-wide monosynaptic inputs to MEC SST^+ neurons via retrograde rabies virus tracing in transgenic SST^{Cre} mice. Most presynaptic neurons were present ipsilaterally in the greater hippocampal-parahippocampal network, with hippocampal CA1 and subiculum containing more than 40% of all counted neurons (Supplementary Fig. 3). These findings point to the hippocampus as an important modulator of MEC SST^+ neurons, likely including those SST^+ neurons that project to LEC.

Target preference of medial entorhinal axons in LEC

We next set out to map functional connections from MEC axons onto neurons in LEC using patch-clamp electrophysiology in acute brain slices. Injections of an AAV vector into MEC of wild-type mice enabled us to tag axons with the light-sensitive cation channel channelrhodopsin2 fused to a yellow fluorescent reporter protein (AAV1-hSyn-ChR2-YFP). Tagged axons were present within the middle, but not the outer, third of the molecular layer of DG (Fig. 2A, left), a pattern consistent with hippocampal innervation by MEC (van Groen et al., 2003). Principal neurons in the superficial layers (layers IIa, IIb and III) of LEC were targeted for somatic whole-cell recordings. These layers are heavily innervated by medial entorhinal axons (Figs. 1F and 2A) and contain the main neuronal populations that project to the hippocampus (van Groen et al., 2003; Kitamura et al., 2014; Ohara et al., 2019).

We recorded membrane currents while depolarizing photosensitive medial entorhinal axons by delivering brief laser pulses of blue light in discrete spots across layers of LEC. The membrane potential of recorded neurons was alternately clamped to the reversal potential for inhibitory and excitatory currents ($V_{INH} = E_{Cl^-} \approx -50$ mV and $V_{EXC} \approx 0$ mV) to isolate excitatory and inhibitory synaptic events, respectively. Optogenetic mapping revealed laser-evoked excitatory postsynaptic currents (EPSCs) and inhibitory postsynaptic currents (IPSCs) in all three groups (PN_{IIA}, PN_{IIB} and PN_{III}; data from 14 mice). To distinguish between monosynaptic and polysynaptic responses, in a subset of experiments, we isolated monosynaptic currents by blocking voltage gated sodium channels with tetrodotoxin (TTX, 1 µM) and voltage gated potassium channels with 4-aminopyridine (4-AP, 100 µM; Petreanu et al. 2009). Some synaptic responses, both excitatory and inhibitory, were intact in PN_{IIA} (EPSC: n = 9 neurons; IPSC: n = 14 neurons; 6 mice), PN_{IIB} (EPSC: n = 10 neurons;

IPSC: 12 neurons; 5 mice) and PNIII (EPSC: n = 15 neurons; IPSC: 13 neurons; 4 mice), confirming that these three populations are postsynaptic partners of axons from MEC (Fig. 2B). In agreement with the pattern of MEC glutamatergic and GABAergic axons, the pharmacological intervention revealed that monosynaptic excitatory inputs could be evoked from both deep and superficial layers, whereas monosynaptic inhibition was most prominent following photostimulation of superficial locations (layers IIb–I; Supplementary Fig. 4).

To further investigate the direct GABAergic input to LEC principal neurons, we isolated monosynaptic inhibitory responses by clamping neurons to the reversal potential for excitatory currents (≈0 mV) while blocking glutamatergic synaptic transmission (DNQX, 10 µM; APV, 50 µM). Under these conditions, there was a clear relationship between the amplitude of recorded inhibitory membrane currents and the location of photostimulation ($p < 0.0001$, Kruskal–Wallis test). Photostimulation of axons within layers I and IIa produced outward currents with amplitudes more than twice as large as those elicited by photostimulation of the other layers (n = 66 neurons from 8 mice, pooled data from PNIIA, PNIIB and PNIII; $p < 0.01$, Kruskal–Wallis multiple comparison test; Figs. 2C and 2D). These were GABAA-mediated chloride currents as they were blocked by the GABAA − antagonist bicuculline (10 µM, n = 11 neurons from 2 mice; Supplementary Fig. 5).

Because MEC SST^+ axons densely innervate layers I/IIa of LEC (Fig. 1F), we sought to directly test whether SST^+ neurons are the source of the observed monosynaptic inhibition. AAV1-FLEX-ChrimsonR-tdTomato was injected into MEC of SST^{Cre} mice (n = 13) to conditionally express the red-shifted channelrhodopsin ChrimsonR in SST^+ neurons. This yielded a dense plexus of photosensitive $ChrimsonR^+$ axons in layer I of LEC (Fig. 2E). Optogenetic axonal activation readily produced outward synaptic currents in PNIIA, but such responses were weaker and less frequently observed among PNIIB and PNIII (Figs. 2F and 2G). To determine whether MEC expresses a target preference for principal neurons in LEC, we analyzed the strength of the synaptic responses by measuring membrane charge transfers evoked by stimulation of photosensitive axons. First, the analyses were restricted to outward currents recorded when the membrane potential was clamped at 0 mV (Fig. 2H). In SST^{Cre} mice, larger charge transfers were found in PNIIA than in PNIIB or PNIII ($p < 0.0001$, Kruskal-Wallis multiple comparison test). Similarly, stronger responses were detected among PNIIA compared to PNIIB and PNIII when monosynaptic inhibitory inputs were

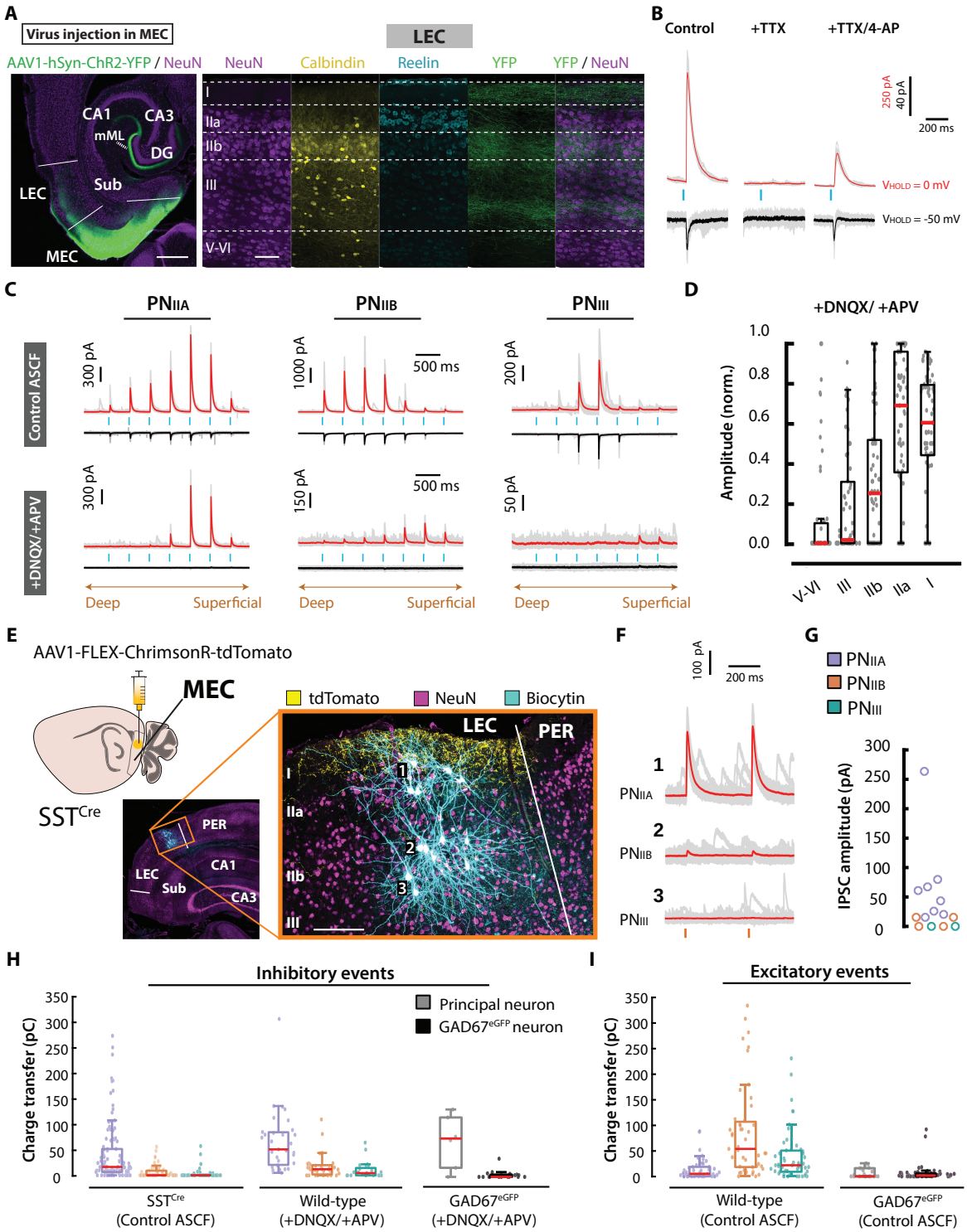

Figure 2. Target preference of medial entorhinal axons in LEC

(A) Left: Virus injection in MEC of a wild-type mouse. Right: High magnification image showing ChR2-expressing axons in LEC. MML, DG middle molecular layer. Scale bars, 500 µm (left) and 100 µm (right). **(B)** Membrane current recordings of a representative PNIIA to the indicated pharmacological treatments during optogenetic stimulation (blue bars). The average membrane current traces (red/black) are superimposed on the individual traces (grey). *(legend continued on next page)*

pharmacologically isolated in wild-type mice (+DNQX/+APV; $p<0.001$, Kruskal-Wallis multiple comparison test; Fig. 2H). Second, when analyses were limited to laser-evoked excitatory events recorded by clamping neurons at -50 mV in wild-type mice, we observed charge transfers with the largest magnitude in PNIIB, followed by PNIII and PNIIA ($p < 0.05$, Kruskal-Wallis multiple comparison test; Fig. 2I).

Lastly, we investigated if GABAergic neurons in LEC are additional recipients of synaptic inputs from MEC. We recorded from GFP^+ GABAergic neurons (n = 51) and principal neurons (17 PNIIA, 2 PNIIB and 4 PNIII) across superficial layers of LEC in $GAD67^{eGFP}$ animals (n = 7) that were injected with AAV1-hSyn-ChrimsonR-tdTomato into MEC (Supplementary Fig. 6). By measuring the average laser-evoked charge transfer, we found that GABAergic neurons had comparably strong excitatory responses to principal neurons ($p = 0.82$, Wilcoxon rank sum test; Fig. 2I and Supplementary Fig. 6). In contrast, the median amplitude of the monosynaptic IPSCs recorded from GABAergic neurons was much smaller than that of principal neurons (+DNQX/+APV; n = 18 tested GABAergic neurons; n = 6 tested principal neurons; $p = 0.0056$, Wilcoxon rank sum test; Fig. 2H and Supplementary Fig. 6). Together, these data indicate that PNIIA receive the strongest inhibition mediated by long-distance SST^+ projections from MEC. In contrast, PNIII / PNIIB are the preferred recipients of excitatory input.

Figure 2 (*continued*). **(C)** Laser-evoked EPSCs (black) and IPSCs (red) in representative PNIIA, PNIIB and PNIII recorded without (top, control ACSF) or with glutamatergic synaptic blockers (bottom, DNQX/APV). **(D)** Normalized IPSC amplitudes plotted against the location of photostimulation. Stimuli that failed to evoke a response are marked as 0. Boxes indicate 25th-75th percentiles, red line is median, whiskers extend to all data points not considered outliers. All data points are superimposed on the box plots. Each value represents data from one cell resulting from photostimulation of the given layer. **(E)** Patch-clamp recorded neurons together with photosensitive MEC SST^+ axons in a semicoronal slice of LEC from an SST^{Cre} mouse. PER, perirhinal cortex. Schematic: Injection to virally label MEC SST^+ neurons with ChrimsonR-tdTomato. Scale bars, 200 µm. **(F)** Membrane current recordings of the numbered neurons in **E** during photostimulation (orange bars). **(G)** Membrane current amplitudes recorded from all neurons in the experiment in **E**. **(H)** Charge transfers in response to optogenetic activation when clamping neurons at 0 mV. Non-responding neurons have charge transfer values of 0 pC. **(I)** Same as in **H**, but for data obtained when clamping neurons to -50 mV.

Target-specific control of postsynaptic neuron activity by medial entorhinal axons in layer I

As layers I/IIa are innervated by axons from both GABAergic and glutamatergic MEC neurons (Fig. 1F), we asked how a combined output of axons in layer I impacts the activity of postsynaptic neurons. In slices prepared from 8 wild-type mice injected with AAV1-hSyn-ChR2-YFP into MEC, we carried out membrane potential recordings of PNIIA, PNIIB and PNIII while optogenetically activating axons in layer I. Recorded neurons were experimentally depolarized to suprathreshold potentials to ensure an adequate driving force for both inhibitory and excitatory synaptic currents (Figs. 3A and 3B).

The most striking difference in optogenetically induced responses was evident for PNIIA versus PNIIB / PNIII, on the population level (Fig. 3) and between single neurons recorded in the same slice (Supplementary Fig. 7). Visual inspection of action potential firing revealed that PNIIA, unlike PNIIB and PNIII, fired very few spikes during blue light illumination (Figs. 3C and 3D). The median number of action potentials emitted by PNIIA decreased to only 19 % of baseline levels (average number of action potentials without laser stimulation) during the first half (0–50 ms) of laser stimulation ($n = 40$, $p < 0.0001$). The median firing activity of PNIIB and PNIII was not different from baseline, but the variability in the number of emitted spikes was high ($p = 0.26$; Wilcoxon signed rank test; Fig. 3E). During the second half (50–100 ms) of laser stimulation, the spiking activity of PNIIA recovered while the firing activity of both PNIIB and PNIII decreased, the latter two showing a median action potential firing of 70% and 87 %, respectively, relative to baseline (PNIIA: $p = 0.54$, PNIIB: $p < 0.0001$, PNIII: $p = 0.02$; Wilcoxon signed rank test; Fig. 3E).

The difference in spiking activity between PNIIA and PNIIB/PNIII matched a clear difference in laser-evoked postsynaptic potentials. Responding PNIIA invariably showed hyperpolarizing deflections of the membrane potential, which in around 10% of PNIIA were accompanied by depolarizing deflections (biphasic response; $n = 5/40$ neurons). Exclusive depolarizing responses were not observed in this neuron group (Figs. 3B and 3F). In contrast, 65% of responding PNIIB and 81% of responding PNIII showed pure depolarizing membrane potential deflections (PNIIB, $n = 28/43$; PNIII, $n = 30/37$). Some responding PNIIB and PNIII showed biphasic responses or solely hyperpolarizing deflections (PNIIB: biphasic, $n = 7/43$;

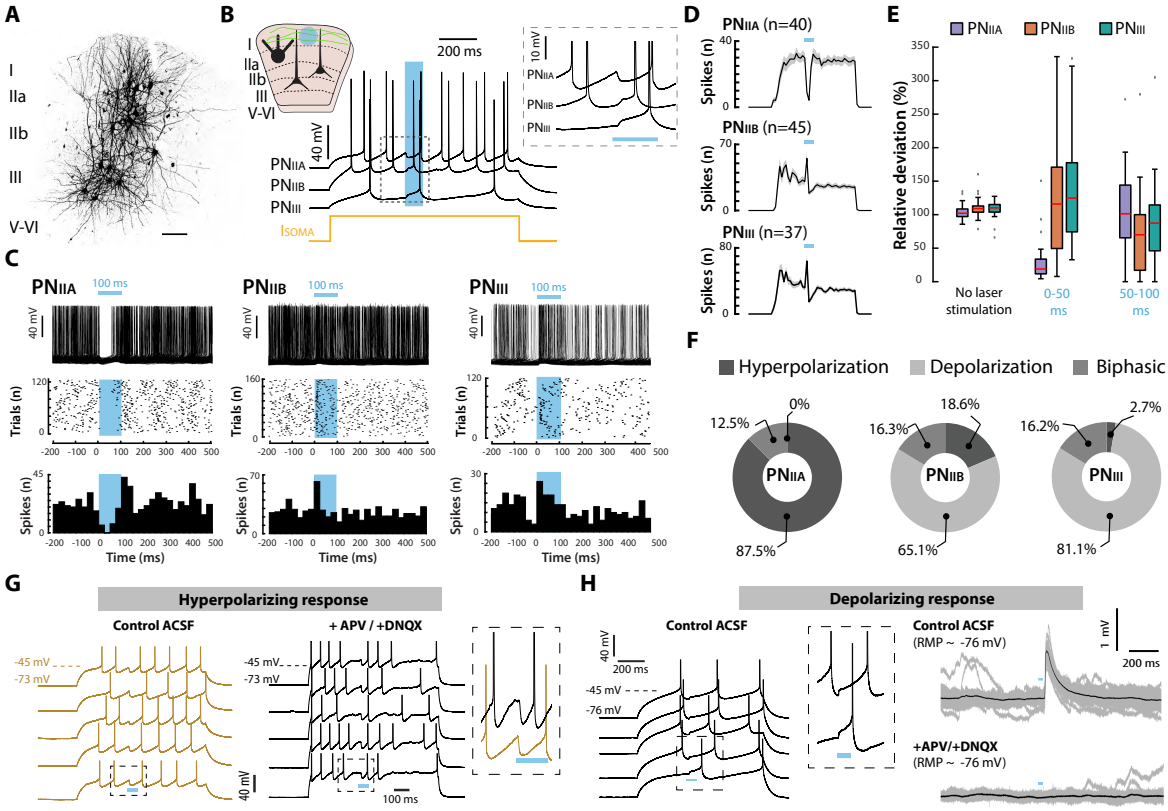

Figure 3. Target-specific control of postsynaptic neuron activity by medial entorhinal axons in layer I

(A) Biocytin-filled principal neurons recorded from layers IIa, IIb and III. Scale bar, 100 µm. **(B)** Different laser-evoked responses of PNIIA versus PNIIB and PNIII (PNIIA, hyperpolarizing; PNIIB, PNIII; depolarizing). Neurons were depolarized by somatic current injections (yellow) while MEC axons were photostimulated with light (blue bar). Schematic: A 100 ms laser stimulation (blue) of MEC axons (ChR2, green) in LEC layer I during current-clamp recordings. **(C)** Action potential firing across multiple sweeps of the photostimulation (blue bar) protocol in representative neurons. Top: Voltage recordings. Middle: Raster plots. Bottom: Histograms. Note the transient suppression of spiking activity in PNIIA and the increase in spiking activity in PNIIB and PNIII during photostimulation. **(D)** Number of action potentials as a function of time. Blue bars are light stimulation. Plots are mean (black) ± standard error of the mean (grey). **(E)** Box plots showing the deviation in action potential firing relative to the average firing activity without laser stimulation. Box plots as in Fig. 2. Outliers are shown as grey points. **(F)** Donut plots showing the proportion of laser-evoked responses. **(G)** Laser-evoked hyperpolarizing responses are resistant to application of glutamatergic synaptic blockers (DNQX/APV). The recording is from a representative PNIIA. **(H)** Laser-evoked depolarizing responses disappear when blocking glutamatergic synaptic transmission. The recording is from a representative PNIII. The membrane potential is indicated for each cell. RMP, resting membrane potential. In the rightmost panels the average voltage trace (black) is overlaid on the individual voltage traces (grey).

hyperpolarizing, n = 8/43; PNIII: biphasic, n = 6/37; hyperpolarizing, n = 1/37; Figs. 3B and 3F).

To assess whether the observed hyperpolarizing responses could reflect local inhibition driven by excitatory MEC inputs, we silenced any contributions from polysynaptic excitatory pathways by eliminating glutamatergic synaptic activity in the slice. Tested laser-evoked hyperpolarizing responses were intact under these conditions (n = 16 neurons from 3 mice), whereas tested depolarizing responses (n = 7 neurons from 3 mice) disappeared (Figs. 3G and 3H). These observations confirm that hyperpolarizing and depolarizing responses reflect the involvement of non-glutamatergic and glutamatergic pathways, respectively. Furthermore, they show that long-range medial entorhinal inhibitory axons, rather than feed-forward inhibition, are responsible for the observed laser-evoked inhibition. Taken together, co-activation of MEC glutamatergic and GABAergic axons in LEC layer I induces a net inhibitory drive to PNIIA and a net excitatory drive to PNIIB or PNIII. Driving input from MEC in layer I therefore produces a selective inhibition of PNIIA and a selective excitation of PNIIB and PNIII.

Pharmacogenetic interrogation of the MEC–LEC inhibitory pathway

We next wondered whether stimulation of MEC SST^+ neurons is sufficient to regulate ongoing activity in LEC layer IIa driven by mice engaging in a behaviorally salient task. Using expression of the immediate early gene cFOS to map neuronal activity, we set out to pharmacogenetically depolarize MEC SST^+ neurons in behaving mice performing a two-choice social memory test previously shown to boost neural activity in LEC (Lopez-Rojas et al., 2022). Because of their GABAergic nature, we hypothesized that depolarizing SST^+ neurons would lead to fewer cFOS-expressing ($cFOS^+$) neurons in layer IIa of LEC. Experimental manipulation restricted to MEC SST^+ neurons was achieved by injecting a Cre-dependent AAV vector encoding the excitatory hM3Dq receptor, a designer receptor exclusively activated by designer drugs (DREADD), unilaterally into MEC of SST^{Cre} mice (n = 7). This resulted in virally tagged SST^+ neurons in MEC along with their long-range projecting axons to LEC (Fig. 4A). Shortly before the behavioral test, clozapine N-oxide (CNO; 10 mg/kg) was administered to depolarize hM3Dq-expressing neurons. To *post hoc* assess the impact of MEC SST^+ activation, we examined the density of $cFOS^+$ neurons in layer IIa of LEC, in slices of ipsilateral LEC containing virus-tagged axons from MEC

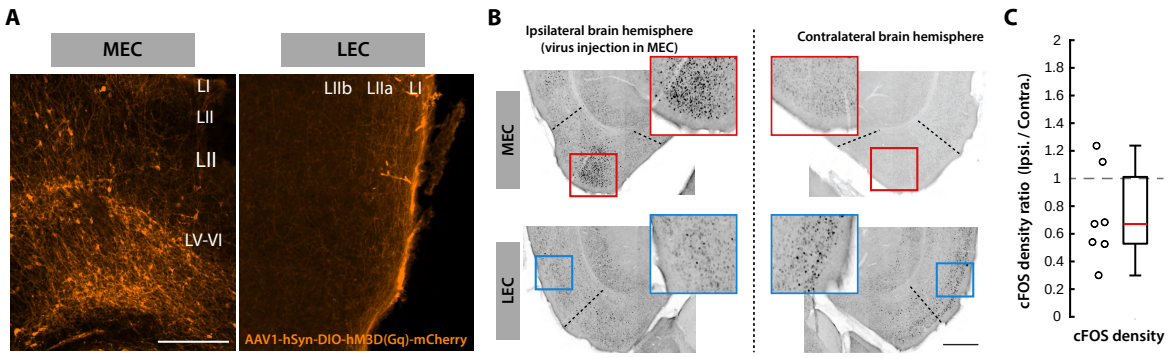

Figure 4. Pharmacogenetic interrogation of the MEC–LEC inhibitory pathway
(A) Left: Viral tagging of MEC SST$^+$ neurons with the excitatory DREADD receptor hM3Dq. Right: Labelled axons in LEC layers I/IIa following virus injection in MEC. **(B)** Example images of cFOS expression in MEC and LEC of both brain hemispheres following DREADD activation of MEC SST$^+$ neurons. Note the abundant cFOS labelling in superficial layers of contralateral LEC as well as the strong cFOS labelling of virally tagged neurons in ipsilateral MEC. **(C)** Quantification of relative density of cFOS$^+$ neurons in layer IIa of LEC between the two brain hemispheres. Most mice displayed a lower density of cFOS$^+$ neurons in LEC receiving inhibitory SST$^+$ input from MEC. Scale bars are 200 µm (**A**) and 500 µm (**B**).

and corresponding portions of contralateral LEC which is devoid of virus-tagged SST$^+$ innervation (Fig. 4B). We observed lower densities of cFOS$^+$ neurons in layer IIa of ipsilateral LEC relative to contralateral LEC in 5 out of 7 mice, as determined by a density ratio (ipsilateral/contralateral) < 1 (Fig. 4C). The median density ratio was 0.67 (0.25 – 1.01 [IQR]) across all mice. Thus, the ipsilateral LEC had a median cFOS density of only two-thirds of the contralateral side, indicating a reduction in neural activity associated with inhibitory SST input from MEC. Although there was not a statistical difference (Wilcoxon signed rank test, p =0.08), our result points to a role for MEC SST neurons in suppressing *in vivo* neuronal activity in LEC layer IIa that warrants further study.

Cortical glutamatergic inputs to principal neurons in layer IIa

In a separate set of experiments, we asked whether inhibitory synaptic responses in PNIIA could also be evoked by activating other cortical areas innervating the superficial layers of LEC. In wild-type mice (n = 3), we first mapped the projection pattern in LEC of three regions previously reported to innervate LEC: the piriform cortex (PIR; Haberly and Price 1978; Kerr et al. 2007), the contralateral LEC (cLEC; Blackstad 1956; Leitner et al. 2016) and the perirhinal cortex (PER; Burwell and Amaral 1998; Doan et al. 2019). We confirmed using anterograde tracing that these areas send axons to the superficial layers of LEC.

Axons from PIR and cLEC were confined almost exclusively to layers I and IIa whereas those from PER terminated diffusely within layers I–III (Fig. 5A). By retrogradely tracing these pathways in 3 GAD67^{eGFP} mice, we observed that 8.6 ± 5.6% (mean ± s.d; 392 / 4651 FG/tdTomato^{+}) neurons in PER and 0.4% ± 0.62 (mean ± s.d; 12 / 1853 FG/tdTomato^{+}) neurons in PIR overlapped with GFP and thus were GABAergic. We did not detect any GFP^{+} GABAergic neurons within the projection from cLEC (518 FG/tdTomato^{+} neurons were counted; Fig. 5B).

To assess synaptic connectivity with PNIIA, in separate wild-type mice, we virally expressed ChR2 in axons from PIR or cLEC. Because of the proximity between PER and the recording location in dorsal LEC, we decided to drive PER activity through patterned laser scanning photostimulation of caged glutamate. Activation of these three pathways while *in vitro* current-clamp recording PNIIA at their resting membrane potential (-67.8 [-69.8 – -66.0] mV; median [IQR]) elicited depolarizing potentials in responding neurons (PER, n = 8 neurons from 4 mice; PIR, n = 32 neurons from 8 mice; cLEC, n = 14 neurons from 6 mice; Fig. 5C). These depolarizing responses were classified as excitatory postsynaptic potentials (EPSPs) as they were observed at voltages positive to the calculated chloride equilibrium potential (≈-69 mV for our solutions). Although delayed inhibitory responses were occasionally observed following the initial EPSP, we did not detect exclusive laser-evoked hyperpolarizing responses. A pharmacological test (+TTX/+4-AP) uncovered that optogenetic activation of axons from PIR or cLEC gave rise to monosynaptic responses in PNIIA (PIR, 6 cells from 1 mouse; cLEC, 3 cells from 1 mouse; Fig. 5C, insets). Taken together, our electrophysiological and anatomical findings indicate that PIR, cLEC and PER provide a prevailing excitatory input to PNIIA.

Our observation that the population of PNIIA receive synaptic inputs from PER, PIR, cLEC as well as MEC suggests that individual LEC PNIIA may integrate synaptic input from several cortical areas. We therefore sought to test in the same experiment whether single PNIIA responds to sequential activation of two upstream brain areas. Synaptic convergence was tested by monitoring the membrane potential of recorded PNIIA while combining stimulation of PER with optogenetic activation of axons from either PIR, cLEC or MEC (PER–PIR/ PER–cLEC/ PER–MEC). To increase the stimulation efficacy of neurons in PER, we replaced glutamate uncaging with extracellular electrical stimulation of the superficial layers of PER, in agreement with the experimental design of a previous study in the rat

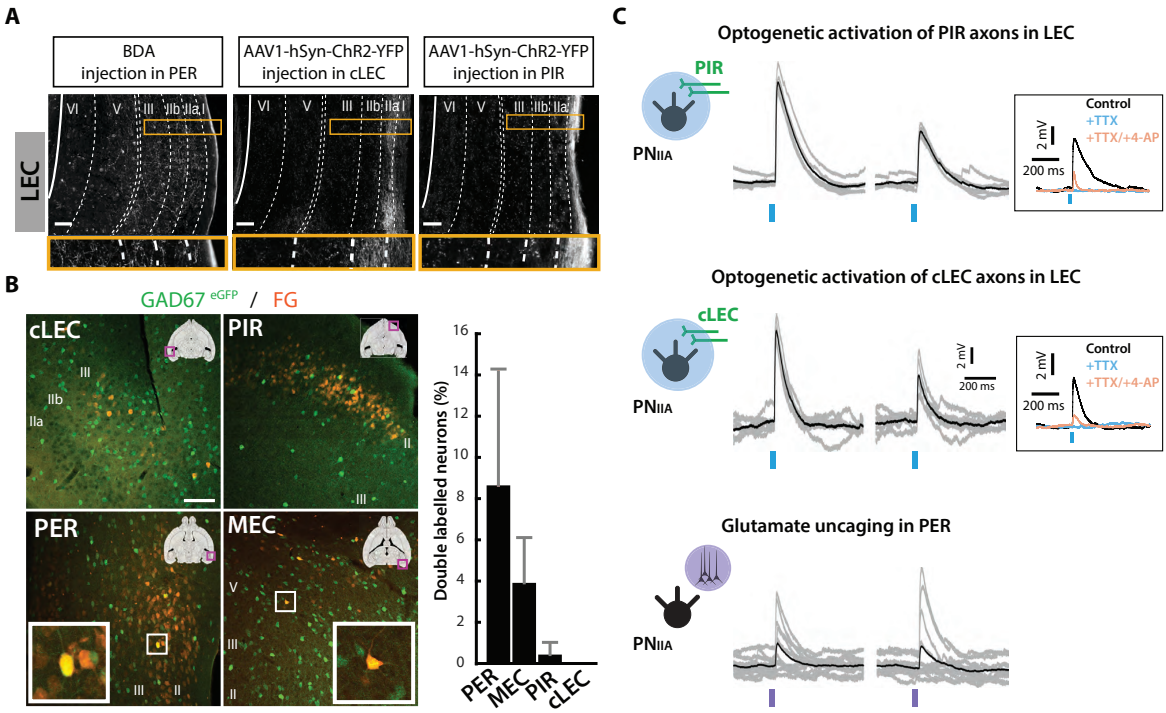

Figure 5. Cortical glutamatergic inputs to principal neurons in layer IIa
(A) Labelled axons in superficial layers of LEC following anterograde tracer injections into PER (left), cLEC (middle) and PIR (right). BDA, biotinylated dextran amine. See Supplementary Fig. 8 for images of the injection sites. **(B)** Confocal images of neurons retrogradely labelled from LEC in a GAD67^{eGFP} mouse (same case as the experiment in Fig. 1A). FG^{+} cell bodies were found in MEC, PER, cLEC and PIR. In this brain, co-localization of GFP and FG was evident in PER and MEC (white square insets). Bar graphs show the proportions of neurons retrogradely labelled with FG or AAV2-CAG-tdTomato that also expressed GFP (FG/tdTomato and GFP; mean ± standard deviation, n = 3 mice). **(C)** Electrophysiological interrogation of afferent pathways in wild-type mice. Optogenetic activation (blue bars) of photosensitive axons from PIR (top) or cLEC (middle) in LEC elicited monosynaptic EPSPs in PNIIA. Insets show average membrane potential traces in control ACSF (black), and ACSF added with TTX (blue) or TTX + 4-AP (orange). Activation of PER neurons (bottom) through UV-photostimulation (purple bars) of caged glutamate evoked EPSPs in PNIIA in LEC. All membrane potential traces show the average trace (black) superimposed on individual trials (grey). Note that the recordings in the three panels are from different mice. Scale bars are 100 µm in (**A**) and (**B**).

(de Villers-Sidani et al., 2004). We found that single PNIIA that responded to PER stimulation often also responded to stimulation of axons from the other tested brain region (PER–PIR: 67.7%, n = 21/31 neurons; PER-cLEC: 77.3%, n = 17/22 neurons; PER–MEC: 59.5%, n = 25/42 neurons), confirming that perirhinal input converges with synaptic inputs from cLEC, PIR and MEC at the level of single PNIIA in LEC (Supplementary Fig. 9).

Synaptic inputs from MEC diminish glutamatergic synaptic events in principal neurons in layer IIa

In a final set of experiments, we tested in 4 wild-type mice how inputs from MEC modulate excitatory synaptic responses in PNIIA evoked by glutamatergic pathways. To this end, we used a dual-color photostimulation approach in order to combine glutamate uncaging with virally-mediated (AAV1-hSyn-ChrimsonR-tdTomato) optogenetics. EPSPs were generated by focal UV-photolysis of caged glutamate at dendrites of PNIIA while synaptic release from MEC was triggered by photostimulation of medial entorhinal ChrimsonR$^+$ axons in layer I of LEC (Fig. 6A). Sequential photorelease of caged glutamate transiently depolarized PNIIA (Fig. 6B), thereby mimicking EPSPs generated by excitatory synaptic inputs from PIR, PER or cLEC. Pairing release of glutamate with photoactivation of MEC axons led to evoked EPSPs that were smaller (middle trace, Fig. 6B) than those generated before and after by photolysis of caged glutamate alone (left and right traces in Fig. 6B; Figs. 6C and 6D). Across the entire set of recordings, synaptic input from MEC reduced the average amplitude as well as the average duration of uncaging-evoked EPSPs ($n = 38$ neurons; amplitude: $p < 0.0001$; duration: $p = 0.0078$; Wilcoxon signed rank test; Figs. 6E–6G). Only in a single PNIIA did we observe that coincident postsynaptic potentials evoked by MEC and experimentally released glutamate summed to a larger amplitude EPSP. These data support the presence of a strong medial entorhinal inhibitory input to PNIIA and further demonstrate that the pathway can reduce the amplitude and duration of concomitant EPSPs arising from excitatory inputs targeting PNIIA dendrites in layer I.

DISCUSSION

In this study, we have identified a circuit linking MEC to neurons in the superficial layers of LEC. The results describe the structural basis for a pathway that may underpin a direct functional interplay between MEC and LEC, one synapse upstream of the hippocampus where, according to common circuit models, information encoded by MEC and LEC is thought to first combine. Our data show that MEC sends both SST$^+$ GABAergic and glutamatergic axons to LEC, where they form functional connections with principal neurons in the superficial layers. By combining slice recordings with optogenetic activation of MEC axons, including a restricted stimulation of SST$^+$ axons in transgenic SST^{Cre} mice, we find

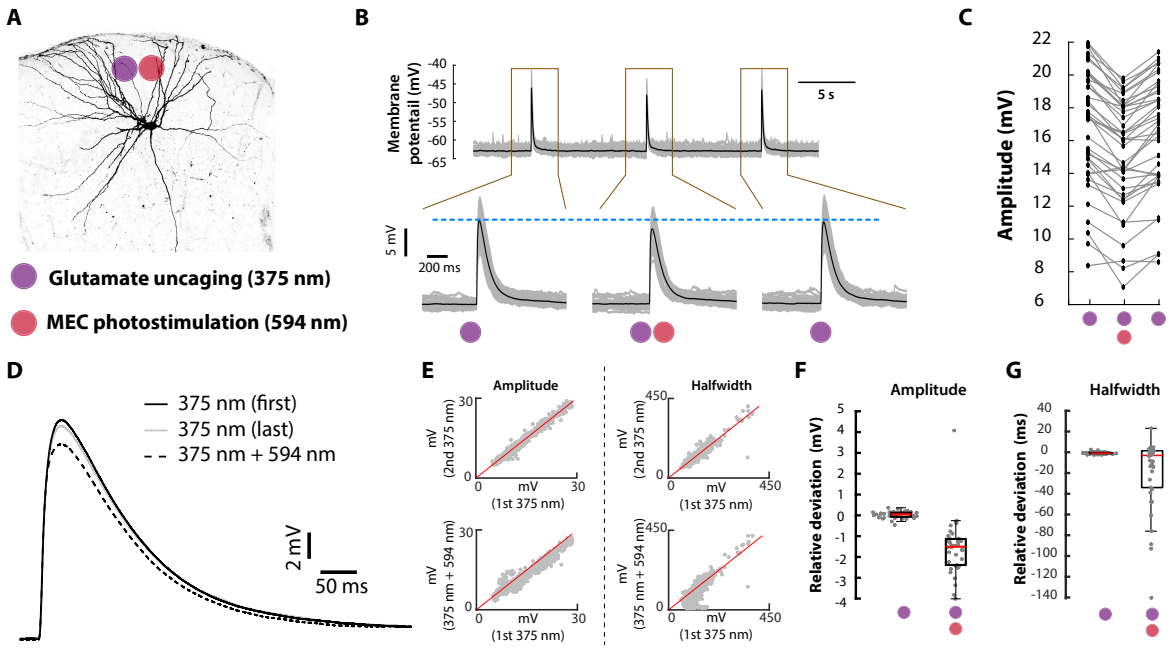

Figure 6. Synaptic inputs from MEC diminish EPSPs of principal neurons in layer IIa
(A) Experimental design of dual photostimulation within layer I of LEC while recording from PNIIA. Depicted is an example of a biocytin-filled PNIIA showing its typical dendritic arborizations in layers I/IIa. **(B)** Example PNIIA recording showing EPSPs evoked by glutamate uncaging alone (left, right) or together with MEC input (middle). The average membrane potential trace (black) is superimposed on the individual traces (grey). The dotted blue line indicates the peak of the average EPSP in response to photolysis of glutamate alone, showing a decrease in EPSP amplitude when pairing glutamate release with MEC activation. **(C)** Quantification of EPSP amplitude for all individual trials recorded from the neuron in **B**. **(D)** Average voltage traces from the recording in **B**. **(E)** Scatter plots of EPSP amplitude (left) and halfwidth (right) for individual sweeps of the experimental protocol from all recorded PNIIA (n = 38). **(F)** Relative deviations in EPSP amplitude between responses elicited when glutamate was released alone (purple) and when glutamate release was paired with photostimulation of MEC axons (purple and red). Data show relative deviations for all recorded PNIIA (n = 38). Box plots as in Fig. 1. **(G)** Same as in **F**, but for EPSP halfwidth.

stronger and more frequent inhibitory responses in PNIIA as compared to the deeper PNIIB and PNIII or local GABAergic neurons. Conversely, excitatory responses are stronger in PNIIB and PNIII than PNIIA.

One of the main discoveries of our work is the circuit that allows MEC to exert direct inhibitory control over LEC principal neurons, especially PNIIA (Fig. 7). Although the SST$^+$ GABAergic neuronal population that project long-range make up only a small proportion out of all LEC-projecting neurons in MEC, they provide a dense and limited innervation of layers I/IIa of LEC. Photostimulation of both glutamatergic and GABAergic axons in layer I,

which contains nearly the entire PNIIA dendritic tree (Tahvildari and Alonso, 2005; Canto and Witter, 2012), led to hyperpolarization of PNIIA. Likewise, we found that synaptic release from MEC axons lead to an overall reduction in the amplitude and duration of EPSPs generated by coincident glutamatergic inputs at dendrites in layer I. These observations indicate that MEC, through projections of SST^+ neurons, mainly drives inhibition in the PNIIA population. The organization of the MEC–LEC inhibitory circuit thus differs from the wiring of most telencephalic circuits, where local GABAergic neurons rather than excitatory neurons are the most common postsynaptic targets of long-distance inhibitory axons (for review see Melzer and Monyer 2020). With the exception of the projection from the hippocampus to the retrosplenial cortex (Yamawaki et al., 2019), local inhibitory neurons are also the main, if not the only, direct recipients of long-range inhibitory input in circuits linking brain areas important for spatial navigation and memory, as shown for inhibitory pathways connecting the hippocampus and MEC (Melzer et al., 2012), the medial septum to MEC (Gonzalez-Sulser et al., 2014; Unal et al., 2015; Fuchs et al., 2016), presubiculum to MEC (van Haeften et al., 1997) and LEC to the hippocampus (Basu et al., 2016). Unlike the present results showing a direct inhibitory influence imparted on LEC PNIIA by MEC SST^+ neurons, activation of those pathways is consistent with disinhibition of principal neurons in the downstream area. Hence, the inhibitory circuit connecting MEC to LEC is likely to play a fundamentally different functional role than other long-range inhibitory circuits in the hippocampal system. While it is generally believed that such circuits participate in synchronization of different brain regions by entraining the activity of local GABAergic neurons (Melzer and Monyer, 2020), our findings implicate an involvement of MEC in gating output from projection neurons in LEC.

It is important to note that LEC receives long-range inhibition also from extra-entorhinal brain areas. While it remains to be determined if PNIIA are postsynaptic partners of GABAergic SST^+ projections from the amygdala (McDonald and Zaric, 2015), a small proportion of PNIIA in LEC had inhibitory, putative monosynaptic, responses upon stimulation of fibers from the medial septum (Desikan et al., 2018). A small population of GABAergic neurons in PER project to LEC, as confirmed in our retrograde tracing experiments, and reportedly target the population of PNIIA (Pinto et al., 2006; Apergis-Schoute et al., 2007). In our slice recordings, however, we did not detect any inhibitory responses in PNIIA upon photolysis of caged glutamate in PER, possibly due to the technical

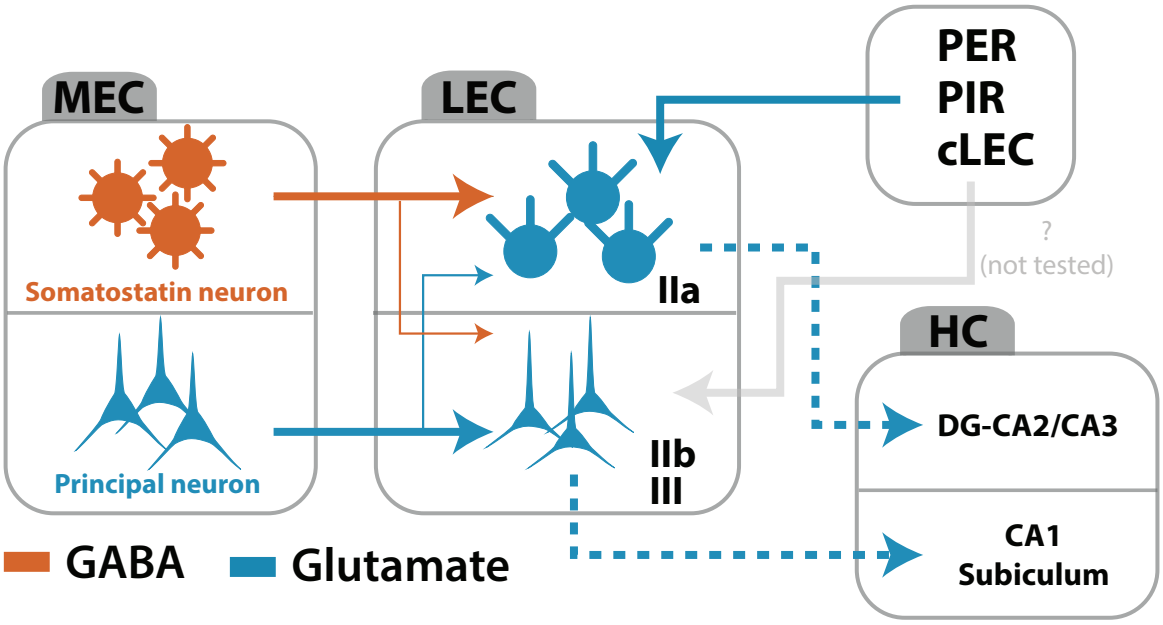

Figure 7. Anatomical organization of the medial entorhinal to lateral entorhinal circuit
Inhibitory and excitatory pathways differentially target principal neurons in the superficial layers of LEC. The main pathways (solid lines) described in this study are shown together with the well-established connectivity between LEC and the hippocampus (dotted lines; Nilssen et al. 2019). For the MEC–LEC pathway, the thickness of the GABAergic/glutamatergic arrows indicate the relative strength of these inputs onto postsynaptic neurons. HC, hippocampus.

difficulty of targeting the relatively few GABAergic neurons projecting to LEC. Although we cannot rule out that PNIIA are targets of long-distance inhibition from PER, similar to previous studies we found that activation of PER elicited EPSPs in recorded PNIIA (Biella et al., 2002a; de Villers-Sidani et al., 2004; Doan et al., 2019). Our results also point to commissural and olfactory pathways as sources of excitatory input to LEC, in line with available anatomical and electrophysiological data (Wilson and Steward, 1978; Leitner et al., 2016; Ohara et al., 2019; Bitzenhofer et al., 2022). Overall, a preferred long-range inhibitory targeting of PNIIA may be a particularly salient feature of the circuit connecting MEC to LEC, rather than a general attribute shared by many cortical connections with LEC. This is corroborated by our observations that SST^+ axons are missing from the return pathway connecting LEC to MEC, indicating that, even in the interplay between the entorhinal subregions, the inhibitory connection is exclusively unidirectional from MEC to LEC. Although other inhibitory neuron types could supply LEC-driven inhibition to MEC, it has recently been reported that the LEC–MEC pathway mainly consists of axons from PNIIA, which provide excitatory synaptic inputs to principal neurons in superficial

layers of MEC (Vandrey et al., 2022). Together, these observations predict that only LEC PNIIA, but not their layer II counterparts in MEC, are under direct inhibitory control by the twin entorhinal subdivision and implies that entorhinal interactions are likely to have a contrasting influence on principal neuron activities in layer II of LEC and MEC.

In line with previous reports (Köhler, 1986; Witter et al., 1986; Dolorfo and Amaral, 1998; Biella et al., 2002b; Chrobak and Amaral, 2007; Ohara et al., 2019), our data show that the MEC pathway targeting LEC originates from neurons in both deep and superficial layers. Although it remains for future *in vivo* studies to determine the functional nature of these projections, some hints may be found in the neuronal composition of the MEC–LEC pathway. Because entorhinal GABAergic neurons projecting to the hippocampus have been found to also distribute local axon collaterals in the EC (Germroth et al., 1989a; Germroth et al., 1989b), it is likely that LEC-projecting GABAergic neurons also innervate nearby neurons to participate in network operations in MEC. We report that MEC-derived direct inhibition to LEC is mediated by axons of SST^+ neurons and not PV^+ neurons, which in MEC are two neuron classes with different laminar distributions (Köhler and Chan-Palay, 1983; Fujimaru and Kosaka, 1996), brain-wide inputs (current findings; Jacobsen 2019) and local connectivity patterns (Fuchs et al., 2016; Kecskés et al., 2020; Fernandez et al., 2022). Pharmacogenetic interventions in behaving mice further show that SST^+ neurons and PV^+ neurons exert an influence over the activity of different types of position-coding cells: aperiodic spatial cells and grid cells, respectively (Miao et al., 2017). Consequently, the inhibitory innervation of LEC limited to SST^+ neurons indicates that neurons in LEC could be preferentially recruited to the network of aperiodic spatial cells in MEC rather than to the network of grid cells. Although the possibility that grid activity is relayed to LEC by excitatory axons from calbindin-expressing neurons (Sun et al., 2015; Zutshi et al., 2018) or neurons in deeper layers (Sargolini et al., 2006) cannot be excluded, a previous observation that MEC reelin-expressing principal neurons, a key anatomical correlate of layer II grid cells (Domnisoru et al., 2013; Gu et al., 2018; Rowland et al., 2018), avoid sending axons to LEC further points to a weak relationship between MEC grid cells and neurons in LEC (Nilssen et al., 2018). In addition, the absence of projections to LEC from MEC PV^+ neurons points to a very limited innervation of LEC by speed cells, which to a large extent have been identified as fast-spiking and putative PV^+ neurons (Kropff et al., 2015; Ye et al., 2018). A population of PV^+ neurons, which includes some that encode running speed, instead

send long-distance axons to the hippocampus (Melzer et al., 2012; Ye et al., 2018). Our current data on inhibitory pathways out of MEC thus point to a substantial difference in the information sent to LEC (via SST^+ neurons) and to the hippocampus (via PV^+ neurons).

An open question with regards to the communication between LEC and the hippocampus is the conditions under which the DG–projecting (i.e., PNIIA) or CA1–projecting (i.e., PNIIB / PNIII) pathways become active. Some upstream brain areas likely influence activity in both main lateral entorhinal-hippocampal pathways. For example, previous studies have shown that axons from olfactory areas (Wouterlood and Nederlof, 1983; Schwerdtfeger et al., 1990), the parasubiculum (Caballero-Bleda and Witter, 1994) and PER (de Villers-Sidani et al., 2004) contact principal neurons in both layers II and III of LEC. Our data show that this holds true also for the MEC–LEC circuit, but it is striking that the presynaptic GABAergic and glutamatergic circuit elements preferentially target postsynaptic neurons in a manner that matches the different connectivity patterns of LEC with the hippocampus (Fig. 7). MEC SST^+ axons mainly connect with PNIIA, which provide input to DG-CA2/CA3 (van Groen et al., 2003; Kohara et al., 2014; Leitner et al., 2016), whereas MEC glutamatergic axons preferentially synapse onto neurons in layers IIb and III, which issue projections to CA1 and subiculum (van Groen et al., 2003; Kitamura et al., 2014; Ohara et al., 2019). It is worth noting that although the hippocampus is generally considered as a main destination of axons of PNIIA and PNIII (Nilssen et al., 2019), the synaptic targets of neurons in layer IIb are reportedly more diverse and include MEC and olfactory areas, in addition to CA1 (Leitner et al., 2016; Ohara et al., 2019). Notwithstanding the heterogeneity in projection targets of PNIIB, the organization of MEC synaptic inputs to LEC as described in this study has two main implications for how MEC might influence lateral entorhinal communication with the hippocampus. First, the weaker relationship between MEC glutamatergic axons and PNIIA as compared to PNIIB and PNIII indicates that activity in the glutamatergic pathway would impose a weaker excitatory influence on lateral entorhinal neurons projecting to DG-CA3/CA2 than on neurons projecting to CA1 and subiculum. Second, the preferred synaptic inhibition onto PNIIA mediated by MEC SST^+ neurons suggests that lateral entorhinal output to DG and CA2-CA3, rather than output to CA1 and subiculum, is under powerful and direct MEC-derived inhibitory control. This organization of MEC inputs to LEC neurons is consistent with the possibility that MEC may route output from LEC by regulating the efficacy by which signals travel to downstream regions of the hippocampus, either through

a suppression of activity in the pathway from layer IIa to DG-CA3/CA2 or a facilitation of activity in the pathway from layers IIb/III to CA1 and subiculum.

ACKNOWLEDGMENTS

We thank Grethe M. Olsen and Bruno Monterotti for technical assistance, and Oscar Chadney for help with the pharmacogenetic experiments. We are also grateful to Anne Nagelhus and Øyvind A. Høydal for discussion and comments on the manuscript. This work was supported by the Research Council of Norway (research grant 227769, the Centre of Excellence scheme - Centre for Neural Computation grant 223262, and the National Infrastructure scheme - NORBRAIN grant 197467) and the Kavli Foundation.

AUTHOR CONTRIBUTIONS

Conceptualization, E.S.N., T.P.D. and M.P.W.; Investigation, E.S.N., B.J. and T.P.D.; Formal analysis, E.S.N., B.J., T.P.D. and P.J.B.G.; Visualization, E.S.N.; Software, P.J.B.G.; Writing – original draft, E.S.N.; Writing – review and editing, E.S.N., B.J., T.P.D., P.J.B.G. and M.P.W.; Supervision, M.P.W.; Funding acquisition, M.P.W.

DECLARATION OF INTERESTS

The authors declare no competing interests.

MATERIALS AND METHODS

Animals

We used transgenic B6.129P2-Pvalb$^{tm1(cre)Arbr}$/J (PV^{Cre}; RRID: IMSR_JAX:017320, The Jackson Laboratory), Sst$^{tm2.1(cre)Zjh}$/J (SST^{Cre}; RRID: IMSR_JAX:013044, The Jackson Laboratory) and Vip$^{tm1(cre)Zjh}$/J (VIP^{Cre}; RRID: IMSR_JAX:010908, The Jackson Laboratory) mice, GAD67^{eGFP} mice (bred in-house; Tamamaki et al. 2003) and wild-type mice (C57BL/6N, RRID: IMSR_CRL:027, Charles River Germany). Both female and male mice were used and randomly selected. All mice were older than 6 weeks at the time of the experiment. Animals were maintained on a 12 hour light / 12 hour dark schedule, and group-housed in transparent acrylic cages with *ad libitum* access to food and water. All experiments were performed in accordance with the Norwegian Animal Welfare Act and the European Convention for the Protection of Vertebrate Animals used for Experimental and Other Scientific Purposes. The experiments were approved by the Norwegian Food Safety Authority (permit no. 8083 and 22312).

Surgeries

Anesthesia was induced by placing the mouse in a chamber filled with isoflurane (5%, 1.2 L/min flow rate; Nycomed Zurich), after which it was mounted in a stereotaxic frame (Kopf Instruments). The animal was placed on a heating pad (37 ℃) to maintain stable body temperature and protective ointment was applied to the eyes. Before the start of surgery, the mouse was given subcutaneous injections of buprenorphine hydrochloride (Temgesic®, 0.1 mg/kg; Indivior) and meloxicam (1 mg/kg; Metacam®, Boehringer Ingelheim Vetmedica), in addition to bupivacaine hydrochloride (1 mg/kg; Marcain™, Astra Zeneca) at the surgical incision site. Anterior-posterior coordinates were measured from bregma (APb) or the posterior transverse sinus (APt), mediolateral (ML) coordinates were measured from the mid-sagittal sinus, and dorso-ventral (DV) coordinates were measured from the dura. Injection sites for all four areas (MEC, cLEC, PIR and PER) were derived from a stereotaxic mouse brain atlas (Franklin and Paxinos, 2007) and adjusted based on an extensive in-house collection of tracing experiments. The following coordinates (in mm) were used: LEC: +1.9 (APt), +4.75 (ML), -2.2 (DV); MEC: +0.50 (APt), +3.10 (ML), -1.8 (DV); PIR: -0.6 (APb), +4.4 (ML), -3.1 (DV); PER: +2.1 (APt), +4.6 (ML), -1.2 (DV). After stereotactic injections, the wound was cleaned and sutured, and the animal was put back in its home cage. All injections were

performed using glass micropipettes. Pressure injections used an automated microinjection pump (Nanoliter 2010, World Precision Instruments) connected to a microsyringe pump controller (Micro4 pump, World Precision Instruments). Iontophoretic injections used a current source driving alternating 6 seconds on/off current (5-15 minutes; 7 µA or 6 µA; Stoelting Midgard).

Anterograde and retrograde chemical tracer injections

Wild-type mice received a single iontophoretic injection of each anterograde tracer: biotinylated dextran amine (BDA; 10 kDa; 5% solution in 0.125 M phosphate buffer, pH 7.4; Thermo Fisher Scientific, Cat. No. D1956) or *Phaseolus vulgaris* leucoagglutinin (PHA-L; 2.5% solution in 10 mM phosphate buffer, pH 7.4; Vector Laboratories, Cat. No. L-1110-5). To reduce the number of animals, the two tracers were deposited in two different cortical areas, i.e., MEC, PER, cLEC or PIR, in the same animal. The retrograde neuroanatomical tracer fluorogold (FG; 2.5% in H_2O, Fluorochrome, ID: Fluorogold) was pressure injected into dorsal LEC, directly ventral to the rhinal fissure, of GAD67^{eGFP} mice.

Virus injections

Each virus was deposited via pressure injection. All virus injections were unilateral. In all cases, 100-300 nL of the virus solution was delivered at 40 nL/min.

Wild-type mice

For optogenetic experiments or anterograde viral tracing in wild-type mice, an injection of AAV1 carrying a fused channelrhodopsin2-YFP protein (AAV1-hSyn-ChR2-H134R-eYFP-WPRE, Addgene, viral prep no. 26973-AAV1) was placed into either MEC, LEC or PIR. For dual-color optogenetic and uncaging experiments, mice were injected with AAV1-hSyn-ChrimsonR-tdTomato (Addgene, viral prep no. 59171-AAV1) into MEC.

SST^{Cre} mice

In SST^{Cre} mice used for optogenetic experiments, AAV1-hSyn-FLEX-ChrimsonR-tdTomato (UNC vector core, deposited by Dr. Ed Boyden) was injected into MEC. For *in vivo* pharmacogenetic manipulation of SST^{+} neurons, AAV1-hSyn-DIO-hM3D(Gq)-mCherry (Addgene, viral prep no. 44361-AAV1) was injected into MEC to conditionally express

the excitatory DREADD receptor hM3Dq. Virus-mediated anterograde tracing from MEC used injections of either AAV1-CAG-FLEX-tdTomato (Addgene, viral prep no. 28306-AAV1) or AAV9-CAG-FLEX-GFP (UNC vector core, deposited by Dr. Ed Boyden), or a mixture consisting of equal amounts of AAV1-CAG-FLEX-tdTomato and AAV1-CamKII-eGFP-WPRE-rBG (Addgene, viral prep no. 105541-AAV1). To specifically label SST$^+$ neurons in LEC, mice received a single injection of AAV1-CAG-FLEX-tdTomato into LEC. For monosynaptic rabies virus tracing, mice were first injected with a helper virus (AAV5-hSyn-FLEX-splitTVA-2A-mCherry-2A-B19G; produced in-house, modified after Addgene plasmid no. 52473) into MEC, and after two weeks they received an injection of an in-house manufactured EnvA pseudotyped G-protein deleted rabies virus expressing GFP in the same anatomical location (see Jacobsen 2019 for details regarding virus production).

PV^{Cre} and VIP^{Cre} mice

To selectively label MEC VIP$^+$ or PV$^+$ neurons, AAV1-CAG-FLEX-tdTomato or AAV5-hSyn-FLEX-splitTVA-2A-mCherry-2A-B19G was injected into MEC of VIP^{Cre} or PV^{Cre} mice, respectively.

GAD67^{eGFP} mice

For optogenetic interrogation of MEC inputs to LEC, AAV1-hSyn-ChrimsonR-tdTomato was injected into MEC. To retrogradely label neurons projecting to LEC, AAV2-CAG-tdTomato (Addgene, viral prep no. 59462-AAV2) was injected into LEC.

Social memory behavioral task

Clozapine-N-oxide (CNO, 10 mg/kg) was administered intraperitoneally 3 weeks post surgery, after which the mice were left to recover for 30 minutes. Mice underwent a two-choice social memory experiment intended to increase neural activity and cFos expression in LEC, as described in detail elsewhere (Lopez-Rojas et al., 2022). In short, the virus-injected mouse (hM3-mouse) was introduced into an arena containing two empty wire cages. After a period of habituation (5 minutes), a novel mouse (N1 and N2) was placed into each cage and the hM3-mouse was allowed to freely explore the arena with the two mice for 5 minutes. The hM3-mouse was then removed for 30 minutes before being reintroduced into the arena. In this case, it was exposed to one of the novel mice previously encountered

(the now familiar N1 mouse) along with a completely novel mouse (N3 mouse). Following the behavioral experiment, the hM3-mouse returned to the home cage for 90 minutes and was thereafter euthanized and the tissue was further processed (see **Immunohistochemistry and imaging**).

Preparation of acute brain slices

Mice of either sex (6-16 weeks old) were used for electrophysiological experiments. For virus-injected animals, acute brain slices were collected 2-4 weeks after surgery. Mice were kept under isoflurane anesthesia until reflexes were no longer observed, after which they were killed by decapitation. The brain was extracted from the skull and submerged in ice-cold (≈0 ℃), continuously oxygenated (95% O_2/5% CO_2), cutting artificial cerebrospinal fluid (ACSF). The cutting ACSF had a composition of 110 mM choline chloride, 2.5 mM KCl, 25 mM D – Glucose, 25 mM $NaHCO_3$, 11.5 mM sodium ascorbate, 3 mM sodium pyruvate, 1.25 mM NaH_2PO_4, 100 mM D – Mannitol, 7 mM $MgCl_2$ and 0.5 mM $CaCl_2$. Osmolality and pH were adjusted to 430 mOsm and 7.4, respectively. The brain hemisphere ipsilateral (for viral injections into PIR or MEC) or contralateral (for viral injections into LEC) to the virus injection site was glued onto the stage of a vibratome (Leica VT1000S, Leica Biosystems). Semicoronal slices (350 µm thickness, 20° tilt with respect to the coronal plane) were acquired. This cutting angle was chosen to preserve the dendritic tree of principal neurons in superficial layers of LEC (Tahvildari and Alonso, 2005; Canto and Witter, 2012) as well as to secure axonal projections from PER to LEC (de Villers-Sidani et al., 2004). Slices were immediately transferred to a heated chamber (35 ℃) and submerged in oxygenated holding ACSF (high Mg^{2+} – low Ca^{2+}) solution containing 126 mM NaCl, 3 mM KCl, 1.2 mM Na_2HPO_4, 10 mM D-glucose, 26 mM $NaHCO_3$, 3 mM $MgCl_2$ and 0.5 mM $CaCl_2$. Slices were maintained at 35℃ for 30 minutes and then allowed to adjust to room temperature until use.

Whole-cell patch-clamp recordings

The slices were moved to a recording rig containing a Axio Examiner.D1 microscope (Carl Zeiss) equipped with a 20x / 1.0 NA water immersion objective and infrared differential interference contrast optics. Patch pipettes (resistance: 2-8 MΩ) were prepared from borosilicate glass capillaries (1.5 outer diameter x 0.86 inner diameter; Harvard Apparatus)

using a Flaming/Brown micropipette puller (P-97; Sutter Instruments) and filled with the appropriate intracellular solution (see below). Patch clamp recordings were performed at 35 ℃ and slices were superfused with oxygenated recording ACSF containing 126 mM NaCl, 3 mM KCl, 1.2 mM Na_2HPO_4, 10 mM D-Glucose, 26 mM $NaHCO_3$, 1.5 mM $MgCl_2$ and 1.6 mM $CaCl_2$. Somata of up to four neurons were targeted for simultaneous recordings. Following the formation of a gigaohm resistance seal between the pipette and the cell membrane, pipette capacitance compensation was performed, and the cell membrane was subsequently ruptured to obtain whole-cell recording configuration. Data were acquired with an EPC 10 Quadro USB amplifier (Heka Elektronik), with amplifier commands and data acquisition controlled by Patchmaster (version 2.90, Heka Elektronik). Acquired data were low-pass (bessel) filtered at 4 kHz and digitized at 10 kHz. In a subset of experiments, bicuculline (10 µM, Sigma-Aldrich, Cat. No. 14343) was introduced to the circulating ACSF to block GABAA-mediated synaptic transmission, whereas combined application of DNQX (10 µM, Tocris Bioscience, Cat. No. 0189) and DL–APV (50 µM, Tocris Bioscience, Cat. No. 0105) was used to block glutamatergic synaptic transmission. Sequential addition of tetrodotoxin (TTX, 1 µM, Tocris Bioscience, Cat. No. 1078) followed by a mixture of both 4-Aminopyridine (4-AP, 100 µM, Sigma-Aldrich, Cat. No. 275875) and TTX was carried out to test whether laser-evoked events reflected monosynaptic inputs (Petreanu et al., 2009).

Voltage clamp

Whole-cell voltage clamp recordings used a cesium-based internal pipette solution (117 mM cesium gluconate, 13 mM CsCl, 2 mM $MgCl_2$, 10 mM HEPES, 10 mM Na_2-phosphocreatine, 0.3 mM Na – GTP, 4 mM Mg – ATP, 5 mM QX314-Cl). Biocytin (Iris Biotech, Cat. No. LS-3510) was added at a concentration of 5–8 mg/mL. Series resistance was continually monitored and maximally compensated (i.e., kept slightly below the compensation level where oscillations start to occur). Recordings with series resistance ≤ 25 MΩ were accepted. In all experiments, we recorded inhibitory postsynaptic currents (IPSCs) and excitatory postsynaptic currents (EPSCs) by clamping the membrane potential to the reversal potential for excitatory currents (E_{EXC} ≈0 mV) and inhibitory, chloride-carried currents (E_{Cl^-} ≈-50 mV), respectively. The holding potentials were corrected for the liquid junction potential (≈10 mV as measured experimentally).

Current clamp

Whole-cell current clamp recordings used a potassium gluconate-based intracellular solution of the following composition: 120 mM K – gluconate, 10 mM KCL, 10 mM Na_2-phosphocreatine, 10 mM HEPES, 4 mM Mg-ATP, 0.3 mM Na-GTP, with pH adjusted to 7.3 and osmolality to 300-305 mOsm. Biocytin (5–8 mg/mL) was added to the internal solution. Online bridge balance adjustments were performed. No correction was carried out for the liquid junction potential (≈13 mV as measured experimentally). In one set of experiments (Fig. 3), a depolarizing step current (500 ms duration) was injected through the pipette into the soma to induce firing of action potentials. The intensity of the applied current was adjusted to the weakest current required to reach threshold and elicit firing of 1-7 action potentials.

Optogenetic activation of photosensitive axons

Laser-scanning photostimulation was accomplished using a UGA-42 GEO point scanning system (Rapp OptoElectronic) equipped with three continuous laser lines (375 nm, 473 nm and 594 nm), and controlled by SysCon software (v. 1.1.8.0, Rapp OptoElectronic). For optogenetic activation of ChR2 or ChrimsonR, the 473 nm or 594 nm diode laser line was used, respectively. The intensity of laser output from the objective was set to ≈8 mW in all experiments using optogenetic activation of ChR2 through injections of AAV1-hSyn-ChR2-H134R-eYFP-WPRE into MEC. To photoactivate virally-expressed ChrimsonR, the laser intensity was set to ≈3 mW (for GAD67^{eGFP} experiments) or ≈4 mW (for SST^{+} experiments). In mice with injections of AAV1-hSyn-ChR2-H134R-eYFP-WPRE into PIR or cLEC, laser intensity (1.5–5.0 mW) was adjusted for each simultaneously recorded neuron cluster, depending on the virus expression levels in the slice, to evoke sub-threshold membrane potential deflections. Laser stimuli were confined to a single location (pulse duration: 100 ms [473 nm]; 10 ms [594 nm]), or they were arranged in a grid pattern consisting of several equidistant stimulation positions (473 nm: one row containing seven stimulation spots or four rows à five spots, pulse duration was 1 ms; 594 nm: one row containing seven stimulation spots, pulse duration was 5 ms). Stimuli were delivered at a frequency of 2 Hz. All 473 nm and 594 nm laser stimuli had a beam diameter of ≈50 µm (light scattering in the medium not taken into account).

Photostimulation of caged glutamate

MNI-caged-L-glutamate (Tocris Bioscience, Cat. No. 1490) was dissolved in 20 mL recording ASCF to a final concentration of 200 µM and recirculated. The solution was replaced when control responses evoked by uncaging near the cell bodies of recorded neurons started to decline in amplitude, or after 3 hours of recirculation (Bendels et al., 2008). Laser-scanning photostimulation of caged glutamate was performed with the same UGA-42 equipment as described above, except here a UV laser (375 nm) was used as light source. The beam diameter of the 375 nm laser stimuli was ≈1 µm. For glutamate uncaging in PER, laser stimuli were administered in a grid pattern (10 x 12 or 21 x 21 stimulation positions), with duration of 5 ms and intensity set to ≈8-9 mW. For uncaging directly at dendrites of principal neurons in layer IIa of LEC, glutamate was released by three repeating laser uncaging events of identical duration and intensity (10 seconds interstimulus interval), with stimulation intensity adjusted for each neuron in order to evoke subthreshold EPSPs. In these experiments, a single pulse of 594 nm laser (50 µm diameter, 10 ms duration, ≈4 mW intensity) was given immediately following the second 375 nm illumination in order to photoactivate ChrimsonR-expressing MEC axons.

Electrical stimulation of perirhinal cortex

Extracellular stimulation of perirhinal cortex was performed with a tungsten bipolar electrode (tip separation: 150-300 µm). The extracellular stimulation electrode was in all cases positioned in the superficial layers of PER adjoining LEC layer IIa, in accordance with anatomical data describing the main projection to dorsolateral LEC originating from layers II and III of PER (Burwell and Amaral, 1998). A single pulse stimulation (100 µs, 0.3-3 mA) was generated by an Iso-Flex isolation unit (AMPI, Israel) controlled by Patchmaster. The stimulation intensity was adjusted for each recording to the minimum current required to evoke postsynaptic potentials in at least one of the simultaneously recorded cells. Experiments in which electrical stimulation failed to produce responses in any of the simultaneously recorded neurons indicated unsuccessful preservation of PER to LEC connectivity, and these were consequently excluded from analysis. The stimulation protocol was repeated 20-50 times.

Immunohistochemistry and imaging

Slices from patch-clamp experiments

Slices were after patch-clamp recordings exposed to 4% paraformaldehyde (PFA, pH 7.4, Sigma-Aldrich, Cat. No. 16005) for 48 hours at 4 ℃, and then rinsed in phosphate buffer (PB, 0.125 M, 4 x 10 min) at room temperature followed by permeabilization in PB containing 0.5% Triton X-100 (PB-Tx, 3 x 15 min). Next, slices were pre-incubated at room temperature for 2 hours in a blocking medium composed of PB-Tx and Normal Goat Serum (NGS, 5% or 10%, Abcam, Cat. No. ab7481), after which they were incubated with primary antibodies (72 hours at 4 ℃; Table 1) in PB-Tx solution.

Table 1. Primary antibodies used in the study

Antibody	Conc.	Supplier	Cat. No	RRID
Chicken anti-GFP	1:500	Abcam	ab13970	AB_300798
Rabbit anti-cFOS	1:500	Abcam	ab190289	AB_2737414
Rabbit anti-2A	1:200	Sigma-Aldrich	ABS31	AB_11214282
Rabbit anti-calbindin	1:3000	Swant	CB38	AB_10000340
Rat anti-SST	1:200	Sigma-Aldrich	MAB354	AB_2255365
Rat anti-RFP	1:500	ChromoTek	5F8	AB_2336064
Guinea pig anti-NeuN	1:1000	Sigma-Aldrich	ABN90P	AB_2341095
Mouse anti-reelin	1:1000	Sigma-Aldrich	MAB5364	AB_11212203
Mouse anti-mCherry	1:500	Clontech	632543	AB_2307319
Goat anti-PHA–L	1:1000	Vector Laboratories	AS-2224-1	AB_2315136

The sections were washed (PB-Tx, 4 x 15 min) and incubated for 24 hours at room temperature in a Pb-Tx solution containing the relevant secondary antibodies (Table 2). Depending on the kind of virally- or genetically encoded fluorescent tag already present in the sample, enhancement of GFP (for GFP/YFP samples) or red fluorescent protein (RFP; for tdTomato samples) was performed. To reveal biocytin-filled neurons, streptavidin conjugated to an Alexa Fluor™ (AF) fluorescent tag (1:400; Thermo Fisher Scientific; AF405 [Cat. No. S32351], AF546 [Cat. No. S11225] or AF633 [Cat. No. S21375]) was added together with the secondary antibodies. In a few samples, NeuroTrace™ 640/660 deep-red fluorescent Nissl (1:200; Thermo Fisher Scientific, Cat. No. N21483) accompanied the secondary antibodies as a cytoarchitectural marker instead of NeuN.

In preparation for confocal microscopy, the slices were first washed in PB (4 x 10 min) at room temperature and dehydrated through a series of increasing ethanol concentrations (30%, 50%, 70%, 90%, 100%, 100%, 10 minutes each). The slices were immersed in a mixture of 100% ethanol and methyl salicylate (1:1, 10 minutes) before being stored in methyl salicylate (VWR Chemicals). Some slices were stored in a cryoprotective solution containing glycerol (20%; VWR Chemicals) and dimethyl sulfoxide (2%; DMSO; VWR Chemicals) without prior dehydration. Slices were mounted in custom made metal slides with the storage solution and coverslipped before being imaged with a laser scanning confocal microscope (LSM 880 AxioImager Z2, Carl Zeiss). Image z-stacks were acquired with Plan-Apochromat objectives (10x, NA 0.45; 20x, NA 0.8) to retrieve the full morphology and location of the biocytin-filled recorded neurons, along with other immunomarkers present in the slice (NeuN/Neurotrace, GFP/tdTomato and reelin/calbindin). AF405 was excited with a 405 diode laser (bandpass emission filter: 410 – 461 nm), AF488 and GFP were excited by the 488 line of an Argon laser (bandpass emission filter: 490 – 543 nm), AF546 and tdTomato/RFP by a DPSS 568 laser line (bandpass emission filter: 570–623 nm), and AF633 by a HeNe 633 laser line (bandpass emission filter: 635-735 nm).

Table 2. Secondary antibodies used in the study

Antibody	Tag	Conc.	Supplier	Cat. No	RRID
Goat anti-chicken	AF488	1:500	Thermo Fisher	A-11039	AB_2534096
Goat anti-rabbit	AF405	1:400	”	A-31556	AB_221605
	AF488	”	”	A-11008	AB_143165
	AF546	”	”	A-11010	AB_2534077
	AF635	”	”	A-31576	AB_2536186
Goat anti-mouse	AF405	1:400	Thermo Fisher	A-31553	AB_221604
	AF488	”	”	A-11001	AB_2534069
	AF546	”	”	A-11003	AB_41370
	AF635	”	”	A-31574	AB_2536184
Goat anti-guinea pig	AF488	1:400	Thermo Fisher	A-11073	AB_2536184
Goat anti-rat	AF546	1:200	Thermo Fisher	A-11081	AB_2534125
Donkey anti-goat	AF546	1:200	Thermo Fisher	A-11056	AB_2534103
Donkey anti-guinea pig	AF405	1:400	Jackson Imm.	706-475-148	AB_2340470

Slices from neuroanatomical and pharmacogenetic experiments

After 7–14 days of survival, virus- or tracer-injected mice were anesthetized with isoflurane gas and euthanized with an overdose of pentobarbital (Apotekerforeningen) administered intraperitoneally, and they were thereafter perfused transcardially first with Ringer's solution (0.85% NaCl, 0.03% KCl, 0.02% $NaHCO_3$, brought to pH 6.9 with CO_2) followed by PFA (4% in PB, pH 7.4). The brain was removed from the skull, postfixed (PFA, 4 ℃, 2-24 hours) and stored in the cryoprotective (DMSO) solution. A freezing microtome was used to cut the brain into horizontal slices (40 µm or 50 µm thickness; 4 or 6 equally spaced series). All sections from brains used for neuroanatomical analysis were treated with the same basic immunohistochemical protocol described for 350 µm sections used in patch clamp experiments, with some modifications. Sections were incubated with the primary antibodies for 48 hours at 4 ℃ and treated with the secondary antibodies for 24 hours at 4℃ or 4 hours in room temperature. Some slices were washed in a Tris buffer (2 x 10 min; 0.61% Tris(hydroxymethyl)aminomethane, pH 7.6) before being mounted on Superfrost slides (Thermo Scientific) from a Tris-gelatin solution (0.2% gelatin in Tris-buffer, pH 7.6). All other slices were washed in a mixture of PB and Tris-HCl (1 x 10 min, 1:1) and subsequently washed in Tris-HCl (2 x 10 min) and mounted on Superfrost slides using Tris-HCl. Finally, the samples were coverslipped with either an entellan/toluene solution or an entellan/xylene solution. To reveal cytoarchitecture for correct brain area identification, a fluorescent NeuN or Nissl stain was used together with labelling for the other immunomarkers, or sections from an adjacent series were stained with cresyl violet (Nissl stain). Coverslipped samples were inspected with fluorescence illumination at the appropriate excitation wavelengths using an Axio Imager M1/2 microscope (Carl Zeiss), and digital images were obtained using an automated fluorescent scanner (Zeiss Axio Scan Z1) rigged with a Plan Apochromat (20x, NA 0.8) objective. The excitation/emission wavelengths were 355-415 nm / 412-438 nm (for FG), 450-488 nm / 501-527 nm (for AF488), 533-558 nm / 583-601 nm (for AF546) and 615-648 nm / 662-756 nm (for AF635). Confocal image z-stacks were acquired from brain sections collected from GAD67^{eGFP} mice injected with a retrograde tracer in LEC. Image scans were taken of MEC, PIR, PER and cLEC using the same settings as described previously (see **Slices from patch-clamp experiments**) in order to visualize the native GFP signal of GAD67^{eGFP} neurons along with retrogradely labelled neurons and SST^{+} neurons.

Brain area identification

In all neuroanatomical tracing experiments, correct placement of tracer injections into the four different areas (MEC, PER, PIR and LEC) was carefully evaluated based on known cytoarchitectonic features (see below). Electrophysiological experiments were initiated after our neuroanatomical experiments had verified the correct surgery coordinates for interrogating pathways to LEC from MEC, PIR, PER and cLEC. In patch-clamp experiments, viral injections were considered to hit the intended target area whenever the axonal innervation patterns in LEC were consistent with the patterns obtained in our neuroanatomical tracing experiments. To ensure that our injections were placed in MEC, without unintended spread to LEC, we examined the innervation patterns in DG. In agreement with the current understanding of entorhinal innervation of DG in rodents (Steward, 1976; van Groen et al., 2003), injections targeting MEC or LEC resulted in axonal labelling in the middle one-third or outer one-third of the molecular layer of DG, respectively. Cases where the injection had clearly spread to LEC, evident from labelling in DG and labelled cell bodies in LEC, were excluded from analysis.

Cytoarchitecture of EC

In this study, EC was divided into LEC and MEC, which in the rodent are distinguished by different cytoarchitectural profiles, hippocampal and extra-hippocampal connectivity patterns as well as functional properties (for review see Nilssen et al. 2019). In short, the mouse EC is a periallocortical region made up of six layers, which includes two cell-sparse layers (I and IV; van Groen 2001). Across the entire EC, lamina dissecans (layer IV) separates deep layers (V-VI) from superficial layers (I-III). The laminar structure is more developed in MEC than in LEC, whereby MEC has a more regular distribution of neurons and a more distinct lamina dissecans. Neurons in the deep layers of MEC are arranged in columns, while layer II features a band of large neurons that are evenly distributed. In LEC, deep layers lack a clear columnnar organization and layer II is generally composed of two sublayers. Layer IIa is located superficial (closer to layer I) to layer IIb and contains a population of large-sized neurons that are irregularly distributed and cluster into islands. At more dorsal locations, layer IIa is separated from the smaller neurons of layer IIb by a cell-free zone. Layer IIb is made up of a densely packed population of neurons, which distinguishes this layer from the loosely arranged zone of scattered neurons in layer III. In LEC of rodents, reelin-expressing neurons distribute in layer IIa whereas calbindin-expressing neurons are

found in layer IIb (Leitner et al., 2016; Nilssen et al., 2018; Doan et al., 2019; Ohara et al., 2019). Most neurons in layer III neither express reelin nor calbindin.

Cytoarchitecture of PIR and PER

PER is a cortical area whose location in the brain is closely associated with the rhinal fissure. Its ventral border is with LEC. A notable distinguishing feature between LEC and PER is the lamina dissecans, which disappears when transitioning from LEC to PER. Furthermore, superficial layers of PER are evenly packed with small neurons, which are replaced in layer IIa of LEC by large reelin-expressing neurons (Cappaert et al., 2015). PIR is characterized as a three-layered allocortex, consisting of an outer molecular layer (layer I) and two subjacent cellular layers. Moreover, PIR overlays the endopirifom nucleus. The three-layered appearance of PIR distinguishes it from surrounding cortical and subcortical structures. In the present study, we did not attempt to further subdivide PIR, although two main divisions (anterior PIR and posterior PIR) are often identified based on heterogeneity in cytoarchitecture and connectivity (Martinez-Garcia et al., 2012).

Data analysis

Electrophysiology

All electrophysiology data analyses were performed off-line using custom-written scripts in Matlab (MathWorks). In voltage-clamp recordings, laser-evoked inward currents recorded near the reversal potential for inhibitory currents (≈-50 mV) were considered excitatory, whereas laser-evoked outward currents recorded near the reversal potential for excitatory currents (≈0 mV) were considered inhibitory. In current clamp recordings, laser-evoked excitatory responses (EPSPs) were depolarizing deflections that were observed at voltages positive to the chloride equilibrium potential (E_{Cl^-} ≈ -69 mV for our solutions). Laser-evoked inhibitory responses (IPSPs) were hyperpolarizing membrane potential deflections. In cases where blockers of glutamatergic/GABAergic synaptic activity were used, the sensitivity of laser-evoked responses to the relevant pharmacological agents was used to aid classification of events as excitatory glutamatergic or inhibitory GABAergic.

In all experiments, the photostimulation protocol was repeated multiple times and the acquired traces were used to produce an average membrane current trace (voltage clamp)

or membrane voltage trace (current clamp). The average trace was used to classify laser-evoked events and extract relevant features (amplitude/charge/halfwidth) of the synaptic event. In some cases (Fig. 6), the amplitude and halfwidth of the synaptic events were also calculated from the individual trials. Events with amplitudes exceeding 10 standard deviations (Z-score = ± 10; Couey et al. 2013; Nilssen et al. 2018) of the baseline and occurring within a 200 ms time window after laser stimulation were classified as true laser-evoked responses (EPSC or IPSC / EPSP or IPSP). Due to the noisy background resulting from concomitant action potential firing, possible laser-evoked postsynaptic potentials in the experiments forming the basis for Fig. 3 were only assessed by visual inspection. In these experiments, depolarizing/hyperpolarizing deflections that were observed in multiple trials (> 10 times) and occurred shortly after laser stimulation (<200 ms) were considered laser-evoked postsynaptic potentials. Baseline was defined as the average membrane current or voltage of a 100 ms time interval prior to laser stimulation onset. The amplitude of the synaptic event was defined as the peak value of the evoked response minus the baseline value. The response halfwidth was taken as the time difference between the rise and fall phases of the synaptic event measured at 50 % amplitude. When calculating amplitude values produced by photostimulation of a given cortical layer (Fig. 2), the amplitudes of all laser-evoked responses in a particular layer were averaged. Values were then normalized by dividing this value by the maximum value of the dataset. To compare response strength across neuron groups, the synaptic charge transfer was measured. This was estimated by calculating the integral of the synaptic current (i.e., the area under the membrane current curve from the onset of laser stimulation until the membrane current returned to baseline). Membrane charge values were calculated for each photostimulation spot that produced a laser-evoked response, and for each responding neuron these values were averaged to yield a representative EPSC/IPSC charge transfer value. For non-responding neurons, i.e., neurons without laser-evoked responses, the membrane charge transfer was defined to be 0 pC.

To quantify the change in the number of emitted action potentials caused by photostimulation (Fig. 3), each recording was partitioned into 25 ms bins and for each bin the average number of action potentials across all repeats of the stimulation protocol was calculated. The relative deviation in firing activity was then calculated as the percentage of action potentials of the laser condition (during photostimulation) relative to the average

number of action potentials in a 650 ms time window without photostimulation. To assess the impact of MEC photostimulation on glutamate uncaging-evoked events, the relative deviation in EPSP amplitude was calculated as the difference in EPSP amplitude (in mV) between the synaptic event evoked by combining uncaging and MEC photostimulation (375 nm + 594 nm stimulation) and the average EPSP amplitude of the two control uncaging stimulations (375 nm stimulation, without MEC photostimulation).

Classification of recorded neurons

During patch-clamp recordings, neurons were initially categorized as belonging to either layer IIa (PNIIA), IIb (PNIIB) or III (PNIII) based on the location of their cell bodies relative to the cytoarchitectural profile of LEC. A final classification was performed *post hoc* by visual inspection of confocal image stacks containing biocytin-filled patch-clamp recorded neurons where the location of these neurons relative to the lamination of NeuN/Nissl cytoarchitecture and/or the distribution of reelin and calbindin was assessed. During slice recordings of GAD67^{eGFP} tissue, GABAergic interneurons were identified based on GFP fluorescence.

Counting of retrogradely labelled neurons

To quantify the amount and nature of long-range GABAergic projections to LEC, retrogradely labelled neurons (FG/tdTomato^{+} neurons) within MEC, PER, cLEC and PIR were manually counted in Neurolucida 360 (MBF Bioscience) using confocal image stacks. To determine the layer distribution of neurons within MEC that had been retrogradely labelled from LEC, scanned images of MEC were inspected and tagged neurons were counted manually using Adobe Illustrator (Adobe Inc.) and assigned to the appropriate MEC layers as revealed by NeuN cytoarchitecture. All images selected for illustration purposes were imported from Zen blue/black software (Zeiss) into Adobe Photoshop (Adobe Inc.) where the contrast and brightness were adjusted.

Counting of rabies-infected neurons

To map monosynaptic inputs to SST^{+} neurons in SST^{Cre} mice, virus-expressing neurons were manually counted using Neurolucida coupled to a fluorescent microscope (Zeiss Axio Imager M1). One series of sections from each brain were used. Neurons expressing

the rabies virus payload were distinguished from neurons expressing the helper virus payload. Neurons that contained markers from both the rabies virus and the helper virus were classified as starter cells, while neurons that expressed only the rabies virus were considered presynaptic neurons to starter cells (monosynaptic input neurons).

Counting of cFOS$^+$ neurons

Images of cFOS$^+$ neurons were obtained from an automated fluorescent scanner as described previously (see **Immunohistochemistry and imaging**) and were subsequently downsampled by a factor of 1:2 and converted from Carl Zeiss file format (.czi) to TIFF file format, under 75% JPEG compression, using customized software (courtesy of Harvard Center for Biological Imaging). The region of interest for neuron counting was layer IIa of LEC in both brain hemispheres. To identify and automatically count cFOS$^+$ neurons, the images of LEC layer IIa were first segmented using a pixel classification strategy in the open-source software Ilastik (version 1.3.2; Berg et al. 2019). A randomly preselected group of eight images were used to train the classifier to correctly identify cFOS$^+$ neurons. The training set included four images from each brain hemisphere (ipsilateral: two for MEC containing the virus injection and two from LEC ipsilateral to the virus injection site; contralateral: two from the contralateral MEC and two from the contralateral LEC). The classifier was trained by manually assigning the content of the training set images into three label classes: "cFOS$^+$ neurons", "Background" and "Artifacts". The classifier was then employed to all LEC layer IIa images by using the Batch Processing function in Ilastik. Ilastik produced binary masks representing the segmentation result, stored in HDF5 file format. The segmented areas were filtered by size and counted using customized Matlab software, producing an absolute number of cFOS$^+$ neurons in the processed material. Densities of cFOS$^+$ neurons were then calculated by dividing the count by the measured area with the use of customized Matlab software. The cFOS$^+$ density values were then averaged across 4-7 sections per animal, yielding an average cFOS$^+$ density value for LEC layer IIa for each mouse.

Statistics

Statistical analyses were carried out in Matlab (MathWorks). Non-parametric statistical hypothesis tests were performed, as all data sets were either small or non-normally distributed as determined by the one-sample Kolmogorov-Smirnov test. All tests were

two-tailed and data were considered significant at $p < 0.05$. The Wilcoxon signed-rank test was used on dependent samples. For independent samples, the Kruskal-Wallis test or the Wilcoxon rank sum test was applied using the multcompare function in Matlab. Bonferroni corrections were used when performing multiple comparisons.

REFERENCES

Apergis-Schoute, J., Pinto, A., and Pare, D. (2007). Muscarinic control of long-range GABAergic inhibition within the rhinal cortices. *J Neurosci* 27, pp. 4061–4071. DOI: 10.1523/JNEUROSCI.0068-07.2007.

Basu, J., Zaremba, J. D., Cheung, S. K., Hitti, F. L., Zemelman, B. V., Losonczy, A., and Siegelbaum, S. A. (2016). Gating of hippocampal activity, plasticity, and memory by entorhinal cortex long-range inhibition. *Science* 351. DOI: 10.1126/science.aaa5694.

Bellmund, J. L., Deuker, L., and Doeller, C. F. (2019). Mapping sequence structure in the human lateral entorhinal cortex. *eLife* 8. DOI: 10.7554/eLife.45333.

Bendels, M. H., Beed, P., Leibold, C., Schmitz, D., and Johenning, F. W. (2008). A novel control software that improves the experimental workflow of scanning photostimulation experiments. *J Neurosci Methods* 175, pp. 44–57. DOI: 10.1016/j.jneumeth.2008.08.010.

Berg, S., Kutra, D., Kroeger, T., Straehle, C. N., Kausler, B. X., Haubold, C., Schiegg, M., Ales, J., Beier, T., Rudy, M., Eren, K., Cervantes, J. I., Xu, B., Beuttenmueller, F., Wolny, A., Zhang, C., Koethe, U., Hamprecht, F. A., and Kreshuk, A. (2019). Ilastik: Interactive Machine Learning for (Bio)Image Analysis. *Nature Methods* 16, pp. 1226–1232. DOI: 10.1038/s41592-019-0582-9.

Biella, G., Uva, L., and de Curtis, M. (2002a). Propagation of neuronal activity along the neocortical-perirhinal-entorhinal pathway in the guinea pig. *J Neurosci* 22, pp. 9972–9979.

Biella, G., Uva, L., Hofmann, U. G., and De Curtis, M. (2002b). Associative interactions within the superficial layers of the entorhinal cortex of the guinea pig. *J Neurophysiol* 88, pp. 1159–1165. DOI: 10.1152/jn.2002.88.3.1159.

Bitzenhofer, S. H., Westeinde, E. A., Zhang, H.-X. B., and Isaacson, J. S. (2022). Rapid odor processing by layer 2 subcircuits in lateral entorhinal cortex. *eLife* 11. DOI: 10.7554/elife.75065.

Blackstad, T. W. (1956). Commissural connections of the hippocampal region in the rat, with special reference to their mode of termination. *J Comp Neurol* 105, pp. 417–537. DOI: 10.1002/cne.901050305.

Bright, I. M., Meister, M. L., Cruzado, N. A., Tiganj, Z., Buffalo, E. A., and Howard, M. W. (2020). A temporal record of the past with a spectrum of time constants in the monkey

entorhinal cortex. *Proc Natl Acad Sci U S A* 117, pp. 20274–20283. DOI: 10.1073/PNAS.1917197117.

Burwell, R. D. and Amaral, D. G. (1998). Perirhinal and postrhinal cortices of the rat: Interconnectivity and connections with the entorhinal cortex. *J Comp Neurol* 391, pp. 293–321. DOI: http://dx.doi.org/10.1002/(SICI)1096-9861(19980216)391:3%3C293::AID-CNE2%3E3.0.CO;2-X.

Caballero-Bleda, M. and Witter, M. P. (1994). Projections from the presubiculum and the parasubiculum to morphologically characterized entorhinal-hippocampal projection neurons in the rat. *Exp Brain Res* 101, pp. 93–108. DOI: 10.1007/BF00243220.

Canto, C. B. and Witter, M. P. (2012). Cellular properties of principal neurons in the rat entorhinal cortex. I. The lateral entorhinal cortex. *Hippocampus* 22, pp. 1256–1276. DOI: 10.1002/hipo.20997.

Cappaert, N. L. M., Van Strien, N. M., and Witter, M. P. (2015). Hippocampal Formation. *The Rat Nervous System*. Ed. by G. Paxinos. 4th ed. San Diego, USA: Academic Press. Chap. 20, pp. 511–573.

Chrobak, J. J. and Amaral, D. G. (2007). Entorhinal cortex of the monkey: VII. intrinsic connections. *J Comp Neurol* 500, pp. 612–633. DOI: 10.1002/cne.21200.

Couey, J. J., Witoelar, A., Zhang, S. J., Zheng, K., Ye, J., Dunn, B., Czajkowski, R., Moser, M. B., Moser, E. I., Roudi, Y., and Witter, M. P. (2013). Recurrent inhibitory circuitry as a mechanism for grid formation. *Nat Neurosci* 16, pp. 318–324. DOI: 10.1038/nn.3310.

Deshmukh, S. S. and Knierim, J. J. (2011). Representation of non-spatial and spatial information in the lateral entorhinal cortex. *Front Behav Neurosci* 5, p. 69. DOI: 10.3389/fnbeh.2011.00069.

Desikan, S., Koser, D. E., Neitz, A., and Monyer, H. (2018). Target selectivity of septal cholinergic neurons in the medial and lateral entorhinal cortex. *Proc Natl Acad Sci U S A* 115, E2644–E2652. DOI: 10.1073/pnas.1716531115.

de Villers-Sidani, E., Tahvildari, B., and Alonso, A. (2004). Synaptic activation patterns of the perirhinal-entorhinal inter-connections. *Neuroscience* 129, pp. 255–265. DOI: 10.1016/j.neuroscience.2004.07.044.

Doan, T. P., Lagartos-Donate, M. J., Nilssen, E. S., Ohara, S., and Witter, M. P. (2019). Convergent Projections from Perirhinal and Postrhinal Cortices Suggest a Multisensory Nature of Lateral, but Not Medial, Entorhinal Cortex. *Cell Rep* 29, pp. 617–627. DOI: 10.1016/j.celrep.2019.09.005.

Dolorfo, C. L. and Amaral, D. G. (1998). Entorhinal cortex of the rat: Organization of intrinsic connections. *J Comp Neurol* 398, pp. 49–82. DOI: https://doi.org/10.1002/(SICI)1096-9861(19980817)398:1%3C49::AID-CNE4%3E3.0.CO;2-9.

Domnisoru, C., Kinkhabwala, A. A., and Tank, D. W. (2013). Membrane potential dynamics of grid cells. *Nature* 495, pp. 199–204. DOI: 10.1038/nature11973.

Fernandez, F. R., Via, G., Canavier, C. C., and White, J. A. (2022). Kinetics and connectivity properties of Parvalbumin- and Somatostatin-positive inhibition in layer 2/3 medial entorhinal cortex. *eNeuro*. DOI: 10.1523/ENEURO.0441-21.2022.

Franklin, K. B. J. and Paxinos, G. (2007). *The Mouse Brain in Stereotactic Coordinates*. 3rd ed. New York, USA: Academic Press.

Fuchs, E. C., Neitz, A., Pinna, R., Melzer, S., Caputi, A., and Monyer, H. (2016). Local and Distant Input Controlling Excitation in Layer II of the Medial Entorhinal Cortex. *Neuron* 89, pp. 194–208. DOI: 10.1016/j.neuron.2015.11.029.

Fujimaru, Y. and Kosaka, T. (1996). The distribution of two calcium binding proteins, calbindin D-28K and parvalbumin, in the entorhinal cortex of the adult mouse. *Neurosci Res* 24, pp. 329–343. DOI: 10.1016/0168-0102(95)01008-4.

Fyhn, M., Molden, S., Witter, M. P., Moser, E. I., and Moser, M. B. (2004). Spatial representation in the entorhinal cortex. *Science* 305, pp. 1258–1264. DOI: 10.1126/science.1099901.

Germroth, P., Schwerdtfeger, W. K., and Buhl, E. H. (1989a). Morphology of identified entorhinal neurons projecting to the hippocampus. A light microscopical study combining retrograde tracing and intracellular injection. *Neuroscience* 30, pp. 683–691. DOI: 10.1016/0306-4522(89)90161-9.

Germroth, P., Schwerdtfeger, W. K., and Buhl, E. H. (1989b). GABAergic neurons in the entorhinal cortex project to the hippocampus. *Brain Research* 494, pp. 187–192. DOI: 10.1016/0006-8993(89)90162-5.

Giocomo, L. M., Stensola, T., Bonnevie, T., Van Cauter, T., Moser, M. B., and Moser, E. I. (2014). Topography of head direction cells in medial entorhinal cortex. *Curr Biol* 24, pp. 252–262. DOI: 10.1016/j.cub.2013.12.002.

Gonzalez-Sulser, A., Parthier, D., Candela, A., McClure, C., Pastoll, H., Garden, D., Sürmeli, G., and Nolan, M. F. (2014). GABAergic projections from the medial septum selectively inhibit interneurons in the medial entorhinal cortex. *J Neurosci* 34, pp. 16739–16743. DOI: 10.1523/JNEUROSCI.1612-14.2014.

Gu, Y., Lewallen, S., Kinkhabwala, A. A., Domnisoru, C., Yoon, K., Gauthier, J. L., Fiete, I. R., and Tank, D. W. (2018). A Map-like Micro-Organization of Grid Cells in the Medial Entorhinal Cortex. *Cell* 175, pp. 1–15. DOI: 10.1016/j.cell.2018.08.066.

Haberly, L. B. and Price, J. L. (1978). Association and commissural fiber systems of the olfactory cortex of the rat. *J Comp Neurol* 178, pp. 711–740. DOI: 10.1002/cne.901780408.

Hafting, T., Fyhn, M., Molden, S., Moser, M. B., and Moser, E. I. (2005). Microstructure of a spatial map in the entorhinal cortex. *Nature* 436, pp. 801–806. DOI: 10.1038/nature03721.

Hargreaves, E. L., Rao, G., Lee, I., and Knierim, J. J. (2005). Major dissociation between medial and lateral entorhinal input to dorsal hippocampus. *Science* 308, pp. 1792–1794. DOI: 10.1126/science.1110449.

Høydal, Ø. A., Skytøen, E. R., Andersson, S. O., Moser, M. B., and Moser, E. I. (2019). Object-vector coding in the medial entorhinal cortex. *Nature* 568, pp. 400–404. DOI: 10.1038/s41586-019-1077-7.

Igarashi, K. M., Lu, L., Colgin, L. L., Moser, M. B., and Moser, E. I. (2014). Coordination of entorhinal-hippocampal ensemble activity during associative learning. *Nature* 510, pp. 143–147. DOI: 10.1038/nature13162.

Jacobs, J., Weidemann, C. T., Miller, J. F., Solway, A., Burke, J. F., Wei, X. X., Suthana, N., Sperling, M. R., Sharan, A. D., Fried, I., and Kahana, M. J. (2013). Direct recordings of grid-like neuronal activity in human spatial navigation. *Nat Neurosci* 16, pp. 1188–1190. DOI: 10.1038/nn.3466.

Jacobsen, B. (2019). Connectivity of Interneurons in the Entorhinal Cortex. PhD thesis. Trondheim, Norway: NTNU.

Kecskés, M., Henn-Mike, N., Agócs-Laboda, Á., Szőcs, S., Petykó, Z., and Varga, C. (2020). Somatostatin expressing GABAergic interneurons in the medial entorhinal cortex preferentially inhibit layer III-V pyramidal cells. *Commun Biol* 3. DOI: 10.1038/s42003-020-01496-x.

Keene, C. S., Bladon, J., McKenzie, S., Liu, C. D., O'Keefe, J., and Eichenbaum, H. (2016). Complementary functional organization of neuronal activity patterns in the perirhinal, lateral entorhinal, and medial entorhinal cortices. *J Neurosci* 36, pp. 3660–3675. DOI: 10.1523/JNEUROSCI.4368-15.2016.

Kerr, K. M., Agster, K. L., Furtak, S. C., and Burwell, R. D. (2007). Functional neuroanatomy of the parahippocampal region: The lateral and medial entorhinal areas. *Hippocampus* 17, pp. 697–708. DOI: 10.1002/hipo.20315.

Kitamura, T., Pignatelli, M., Suh, J., Kohara, K., Yoshiki, A., Abe, K., and Tonegawa, S. (2014). Island cells control temporal association memory. *Science* 343, pp. 896–901. DOI: 10.1126/science.1244634.

Kohara, K., Pignatelli, M., Rivest, A. J., Jung, H. Y., Kitamura, T., Suh, J., Frank, D., Kajikawa, K., Mise, N., Obata, Y., Wickersham, I. R., and Tonegawa, S. (2014). Cell type-specific genetic and optogenetic tools reveal hippocampal CA2 circuits. *Nat Neurosci* 17, pp. 269–279. DOI: 10.1038/nn.3614.

Köhler, C. (1988). Intrinsic connections of the retrohippocampal region in the rat brain: III. The lateral entorhinal area. *J Comp Neurol* 271, pp. 208–228. DOI: 10.1002/cne.902710204.

Köhler, C. (1986). Intrinsic connections of the retrohippocampal region in the rat brain. II. The medial entorhinal area. *J Comp Neurol* 246, pp. 149–169. DOI: 10.1002/cne.902460202.

Köhler, C. and Chan-Palay, V. (1983). Somatostatin and vasoactive intestinal polypeptide-like immunoreactive cells and terminals in the retrohippocampal region of the rat brain. *Anat Embryol* 167, pp. 151–172. DOI: 10.1007/BF00298508.

Kropff, E., Carmichael, J. E., Moser, M. B., and Moser, E. I. (2015). Speed cells in the medial entorhinal cortex. *Nature* 523, pp. 419–424. DOI: 10.1038/nature14622.

Leitner, F. C., Melzer, S., Lütcke, H., Pinna, R., Seeburg, P. H., Helmchen, F., and Monyer, H. (2016). Spatially segregated feedforward and feedback neurons support differential odor processing in the lateral entorhinal cortex. *Nat Neurosci* 19, pp. 935–944. DOI: 10.1038/nn.4303.

Lopez-Rojas, J., de Solis, C. A., Leroy, F., Kandel, E. R., and Siegelbaum, S. A. (2022). A direct lateral entorhinal cortex to hippocampal CA2 circuit conveys social information required for social memory. *Neuron*. DOI: 10.1016/j.neuron.2022.01.028.

Martinez-Garcia, F., Novejarque, A., Gutierrez-Castellanos, and Lanuza, E. (2012). Piriform Cortex and Amygdala. *The Mouse Nervous System*. Ed. by C. Watson, G. Paxinos, and L. Puelles. 1st ed. Elsevier Inc. Chap. 6, pp. 140–168.

McDonald, A. J. and Zaric, V. (2015). GABAergic somatostatin-immunoreactive neurons in the amygdala project to the entorhinal cortex. *Neuroscience* 290, pp. 227–242. DOI: 10.1016/j.neuroscience.2015.01.028.

Melzer, S., Michael, M., Caputi, A., Eliava, M., Fuchs, E. C., Whittington, M. A., and Monyer, H. (2012). Long-range-projecting GABAergic neurons modulate inhibition in hippocampus and entorhinal cortex. *Science* 335, pp. 1506–1510. DOI: 10.1126/science.1217139.

Melzer, S. and Monyer, H. (2020). Diversity and function of corticopetal and corticofugal GABAergic projection neurons. *Nat Rev Neurosci* 21, pp. 499–515. DOI: 10.1038/s41583-020-0344-9.

Miao, C., Cao, Q., Moser, M. B., and Moser, E. I. (2017). Parvalbumin and Somatostatin Interneurons Control Different Space-Coding Networks in the Medial Entorhinal Cortex. *Cell* 171, 507–521 e17. DOI: 10.1016/j.cell.2017.08.050.

Montchal, M. E., Reagh, Z. M., and Yassa, M. A. (2019). Precise temporal memories are supported by the lateral entorhinal cortex in humans. *Nat Neurosci* 22, pp. 284–288. DOI: 10.1038/s41593-018-0303-1.

Nilssen, E. S., Jacobsen, B., Fjeld, G., Nair, R. R., Blankvoort, S., Kentros, C., and Witter, M. P. (2018). Inhibitory connectivity dominates the fan cell network in layer II of lateral entorhinal cortex. *J Neurosci* 38, pp. 9712–9727. DOI: 10.1523/JNEUROSCI.1290-18.2018.

Nilssen, E. S., Doan, T. P., Nigro, M. J., Ohara, S., and Witter, M. P. (2019). Neurons and networks in the entorhinal cortex: A reappraisal of the lateral and medial entorhinal subdivisions mediating parallel cortical pathways. *Hippocampus* 29, pp. 1238–1254. DOI: 10.1002/hipo.23145.

Ohara, S., Gianatti, M., Itou, K., Berndtsson, C. H., Doan, T. P., Kitanishi, T., Mizuseki, K., Iijima, T., Tsutsui, K. I., and Witter, M. P. (2019). Entorhinal Layer II Calbindin-Expressing Neurons Originate Widespread Telencephalic and Intrinsic Projections. *Front Syst Neurosci* 13. DOI: 10.3389/fnsys.2019.00054.

Petreanu, L., Mao, T., Sternson, S. M., and Svoboda, K. (2009). The subcellular organization of neocortical excitatory connections. *Nature* 457, pp. 1142–1145. DOI: 10.1038/nature07709.

Pinto, A., Fuentes, C., and Pare, D. (2006). Feedforward inhibition regulates perirhinal transmission of neocortical inputs to the entorhinal cortex: ultrastructural study in guinea pigs. *J Comp Neurol* 495, pp. 722–734. DOI: 10.1002/cne.20905.

Rodo, C., Sargolini, F., and Save, E. (2017). Processing of spatial and non-spatial information in rats with lesions of the medial and lateral entorhinal cortex: Environmental complexity matters. *Behav Brain Res* 320, pp. 200–209. DOI: 10.1016/j.bbr.2016.12.009.

Rowland, D. C., Obenhaus, H. A., Skytøen, E. R., Zhang, Q., Kentros, C. G., Moser, E. I., and Moser, M. B. (2018). Functional properties of stellate cells in medial entorhinal cortex layer II. *eLife* 7, e36664. DOI: 10.7554/eLife.36664.

Sargolini, F., Fyhn, M., Hafting, T., McNaughton, B. L., Witter, M. P., Moser, M. B., and Moser, E. I. (2006). Conjunctive representation of position, direction, and velocity in entorhinal cortex. *Science* 312, pp. 758–762. DOI: 10.1126/science.1125572.

Savelli, F., Yoganarasimha, D., and Knierim, J. J. (2008). Influence of boundary removal on the spatial representations of the medial entorhinal cortex. *Hippocampus* 18, pp. 1270–1282. DOI: 10.1002/hipo.20511.

Schwerdtfeger, W. K., Buhl, E. H., and Germroth, P. (1990). Disynaptic olfactory input to the hippocampus mediated by stellate cells in the entorhinal cortex. *J Comp Neurol* 292, pp. 163–177. DOI: 10.1002/cne.902920202.

Solstad, T., Boccara, C. N., Kropff, E., Moser, M. B., and Moser, E. I. (2008). Representation of geometric borders in the entorhinal cortex. *Science* 322, pp. 1865–1868. DOI: 10.1126/science.1166466.

Steward, O. (1976). Topographic organization of the projections from the entorhinal area to the hippocampal formation of the rat. *J Comp Neurol* 167, pp. 285–314. DOI: 10.1002/cne.901670303.

Sugar, J. and Moser, M. B. (2019). Episodic memory: Neuronal codes for what, where, and when. *Hippocampus* 29, pp. 1190–1205. DOI: 10.1002/hipo.23132.

Sun, C., Kitamura, T., Yamamoto, J., Martin, J., Pignatelli, M., Kitch, L. J., Schnitzer, M. J., and Tonegawa, S. (2015). Distinct speed dependence of entorhinal island and ocean cells, including respective grid cells. *Proc Natl Acad Sci U S A* 112, pp. 9466–9471. DOI: 10.1073/pnas.1511668112.

Swanson, L. W. and Köhler, C. (1986). Anatomical evidence for direct projections from the entorhinal area to the entire cortical mantle in the rat. *J Neurosci* 6, pp. 3010–3023. DOI: 10.1523/jneurosci.06-10-03010.1986.

Tahvildari, B. and Alonso, A. (2005). Morphological and electrophysiological properties of lateral entorhinal cortex layers II and III principal neurons. *J Comp Neurol* 491, pp. 123–140. DOI: 10.1002/cne.20706.

Tamamaki, N., Yanagawa, Y., Tomioka, R., Miyazaki, J. I., Obata, K., and Kaneko, T. (2003). Green Fluorescent Protein Expression and Colocalization with Calretinin, Parvalbumin, and Somatostatin in the GAD67-GFP Knock-In Mouse. *J Comp Neurol* 467, pp. 60–79. DOI: 10.1002/cne.10905.

Tsao, A., Moser, M. B., and Moser, E. I. (2013). Traces of experience in the lateral entorhinal cortex. *Curr Biol* 23, pp. 399–405. DOI: 10.1016/j.cub.2013.01.036.

Tsao, A., Sugar, J., Lu, L., Wang, C., Knierim, J. J., Moser, M. B., and Moser, E. I. (2018). Integrating time from experience in the lateral entorhinal cortex. *Nature* 561, pp. 57–62. DOI: 10.1038/s41586-018-0459-6.

Unal, G., Joshi, A., Viney, T. J., Kis, V., and Somogyi, P. (2015). Synaptic targets of medial septal projections in the hippocampus and extrahippocampal cortices of the mouse. *J Neurosci* 35, pp. 15812–15826. DOI: 10.1523/JNEUROSCI.2639-15.2015.

Vandrey, B., Armstrong, J., Brown, C. M., Garden, D. L. F., and Nolan, M. F. (2022). Fan cells in lateral entorhinal cortex directly influence medial entorhinal cortex through synaptic connections in layer 1. *bioRxiv*, pp. 1–50. DOI: https://doi.org/10.1101/2022.08.25.505296.

van Groen, T. (2001). Entorhinal cortex of the mouse: cytoarchitectonical organization. *Hippocampus* 11, pp. 397–407. DOI: 10.1002/hipo.1054.

van Groen, T., Miettinen, P., and Kadish, I. (2003). The entorhinal cortex of the mouse: Organization of the projection to the hippocampal formation. *Hippocampus* 13, pp. 133–149. DOI: 10.1002/hipo.10037.

van Haeften, T., Wouterlood, F. G., Jorritsma-Byham, B., and Witter, M. P. (1997). GABAergic presubicular projections to the medial entorhinal cortex of the rat. *J Neurosci* 17, pp. 862–874. DOI: 10.1523/jneurosci.17-02-00862.1997.

Wang, C., Chen, X., Lee, H., Deshmukh, S. S., Yoganarasimha, D., Savelli, F., and Knierim, J. J. (2018). Egocentric coding of external items in the lateral entorhinal cortex. *Science* 362, pp. 945–949. DOI: 10.1126/science.aau4940.

Wilson, R. C. and Steward, O. (1978). Polysynaptic activation of the dentate gyrus of the hippocampal formation: an olfactory input via the lateral entorhinal cortex. *Exp Brain Res* 33, pp. 523–534.

Witter, M. P., Room, P., Groenewegen, H. J., and Lohman, A. H. (1986). Connections of the parahippocampal cortex in the cat. V. Intrinsic connections; comments on input/output

connections with the hippocampus. *J Comp Neurol* 252, pp. 78–94. DOI: 10.1002/cne.902520105.

Wouterlood, F. G. and Nederlof, J. (1983). Terminations of olfactory afferents on layer II and III neurons in the entorhinal area: Degeneration-golgi-electron microscopic study in the rat. *Neurosci Lett* 36, pp. 105–110. DOI: 10.1016/0304-3940(83)90250-1.

Xu, W. and Wilson, D. A. (2012). Odor-evoked activity in the mouse lateral entorhinal cortex. *Neuroscience* 223, pp. 12–20. DOI: 10.1016/j.neuroscience.2012.07.067.

Yamawaki, N., Li, X., Lambot, L., Ren, L. Y., Radulovic, J., and Shepherd, G. M. (2019). Long-range inhibitory intersection of a retrosplenial thalamocortical circuit by apical tuft-targeting CA1 neurons. *Nature Neuroscience* 22, pp. 618–626. DOI: 10.1038/s41593-019-0355-x.

Yartsev, M. M., Witter, M. P., and Ulanovsky, N. (2011). Grid cells without theta oscillations in the entorhinal cortex of bats. *Nature* 479, pp. 103–107. DOI: 10.1038/nature10583.

Ye, J., Witter, M. P., Moser, M. B., and Moser, E. I. (2018). Entorhinal fast-spiking speed cells project to the hippocampus. *Proc Natl Acad Sci U S A* 115, E1627–E1636. DOI: 10.1073/pnas.1720855115.

Yoganarasimha, D., Rao, G., and Knierim, J. J. (2011). Lateral entorhinal neurons are not spatially selective in cue-rich environments. *Hippocampus* 21, pp. 1363–1374. DOI: 10.1002/hipo.20839.

Zutshi, I., Fu, M. L., Lilascharoen, V., Leutgeb, J. K., Lim, B. K., and Leutgeb, S. (2018). Recurrent circuits within medial entorhinal cortex superficial layers support grid cell firing. *Nat Commun* 9, p. 3701. DOI: 10.1038/s41467-018-06104-5.

SUPPLEMENTARY MATERIAL

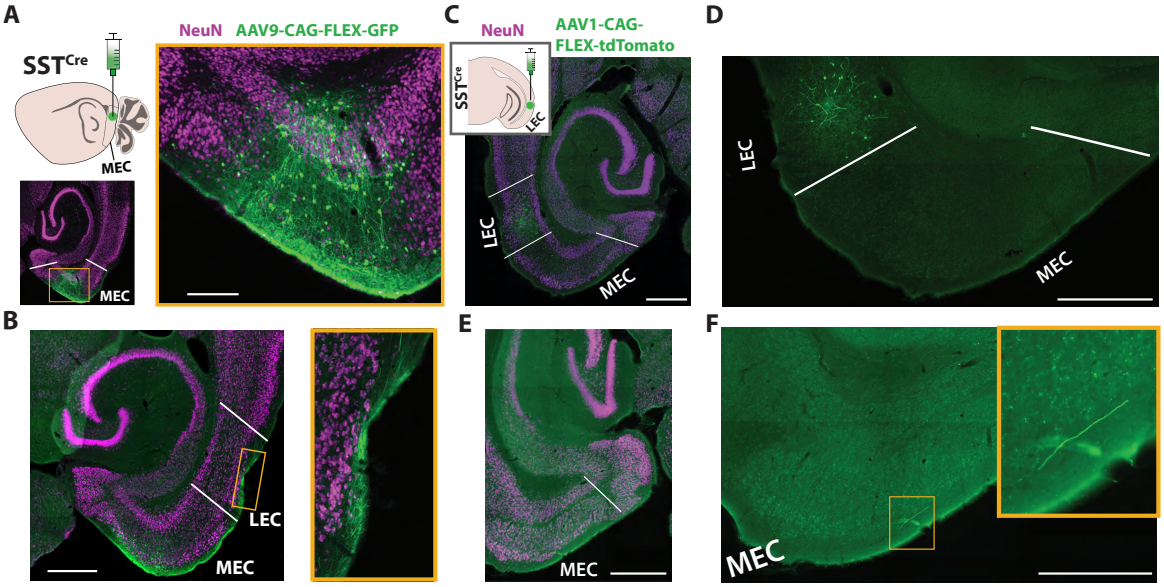

Supplementary Figure 1. SST$^+$ neurons project from MEC to LEC, but only very sparsely in the opposite direction, from LEC to MEC

(A) Conditional labelling of SST$^+$ neurons through injection of AAV9-CAG-FLEX-GFP into MEC of an SST^{Cre} mouse. **(B)** Labelling of MEC SST$^+$ neurons as shown in **A** gives rise to an axonal projection innervating the most superficial layers of LEC. **(C)** Same as in **A**, but for an injection of the Cre-dependent virus AAV1-CAG-FLEX-tdTomato into LEC. **(D)** Processes of labelled LEC SST$^+$ neurons, as shown in **C**, were confined to LEC, with no transport to neighboring MEC. **(E, F)** A horizontal section through dorsal MEC of the experiment shown in **C** and **D**. The boxed region points to a single labelled LEC SST$^+$ axon in MEC. Scale bars are 250 µm (**A**), 1000 µm (**B**) and 500 µm (**C–F**).

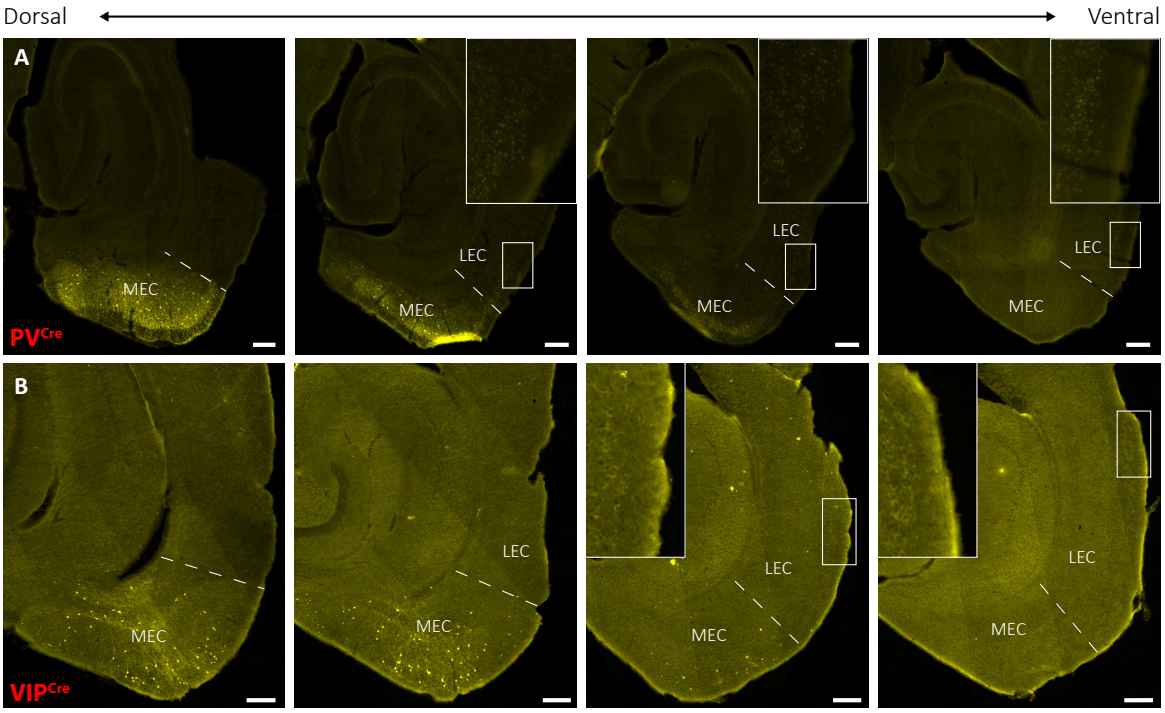

Supplementary Figure 2. Medial entorhinal PV⁺ neurons and VIP⁺ neurons do not innervate LEC. **(A)** An injection of AAV5-hSyn-FLEX-splitTVA-2A-mCherry-2A-B19G into MEC of a PV^{Cre} mouse labels specifically PV^{+} neurons. Labelled processes were confined to MEC, and no labelling was evident in neighboring LEC. **(B)** Same as **A**, but for the specific labelling of VIP^{+} neurons in a VIP^{Cre} mouse using the Cre-dependent virus AAV1-CAG-FLEX-tdTomato. All scale bars are 200 µm.

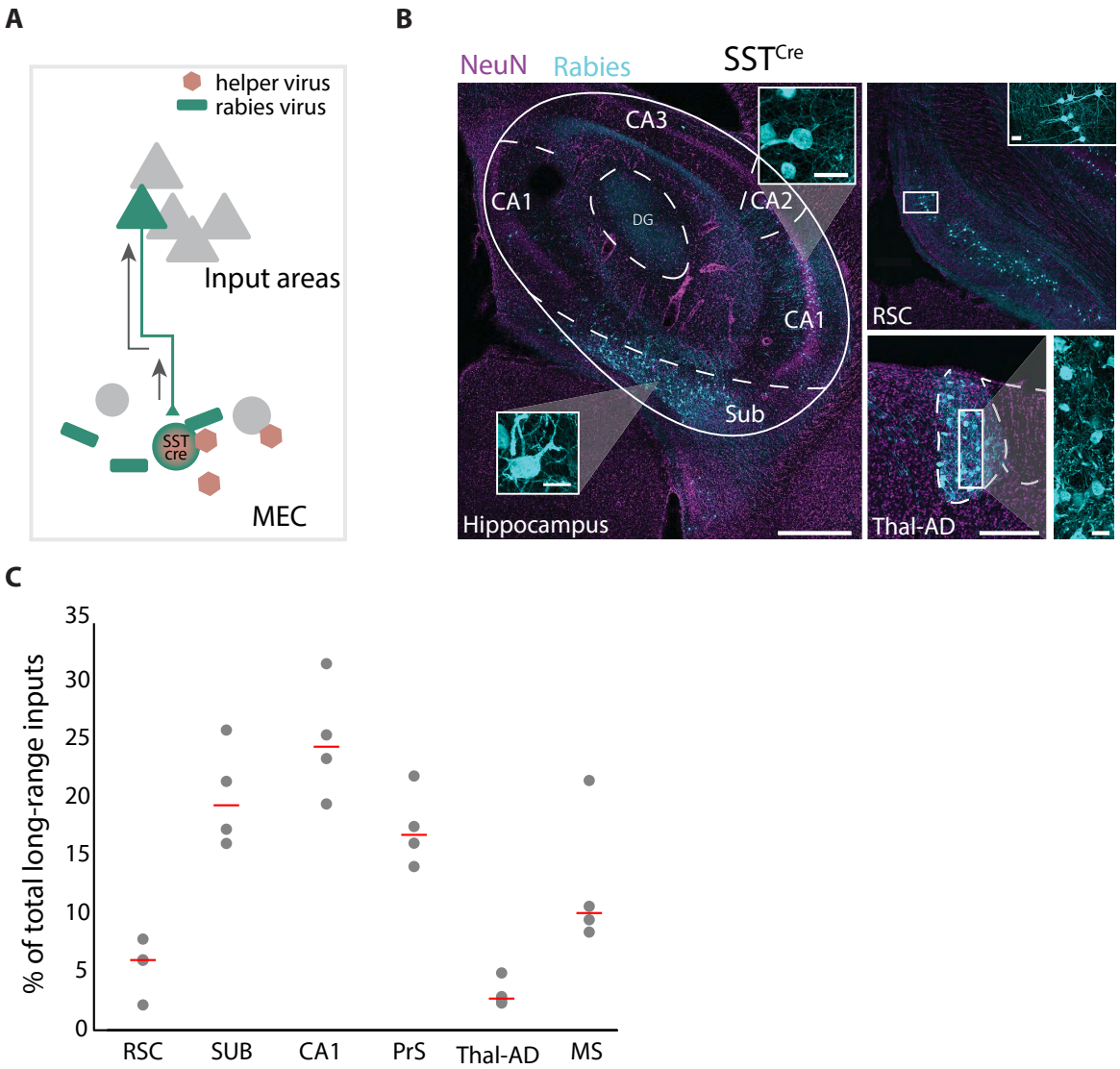

Supplementary Figure 3. Monosynaptic input tracing to MEC SST⁺ neurons
(A) Experiment using rabies virus to trace monosynaptic inputs to SST⁺ neurons in MEC of SST^{Cre} mice. **(B)** Rabies-expressing neurons in the hippocampus, retrosplenial cortex (RSC) and the anterodorsal thalamic nucleus (Thal-AD) that are presynaptic to MEC SST⁺ neurons. Scale bars are 200 µm and 20 µm (insets). **(C)** Neuron counts showing the 6 brain areas with most rabies-infected neurons. PrS, presubiculum. MS, medial septum. Data from 4 mice.

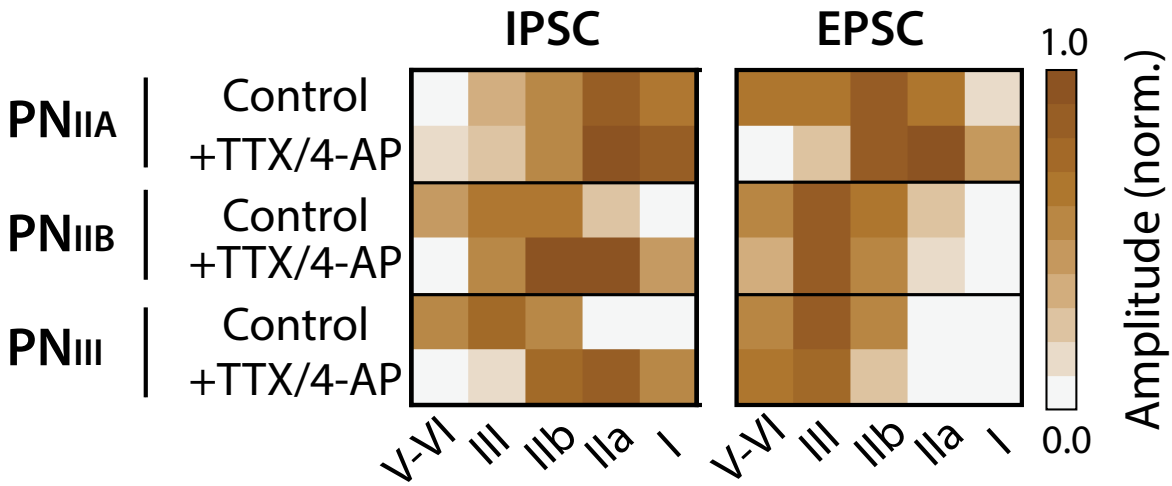

Supplementary Figure 4. Layer-dependent distribution of excitatory and inhibitory synaptic inputs

Heatmaps of median membrane current amplitudes (normalized values) of neurons recorded in layers IIa, IIb, and III as a function of the layer of photostimulation (X axis). These color-coded excitation- and inhibition profiles based on the median normalized EPSC/IPSC amplitude values were calculated from all groups of responding principal neurons recorded in the presence of control ACSF and ACSF added with TTX/4-AP. The anatomical layer associated with each photostimulation position was determined post-recording.

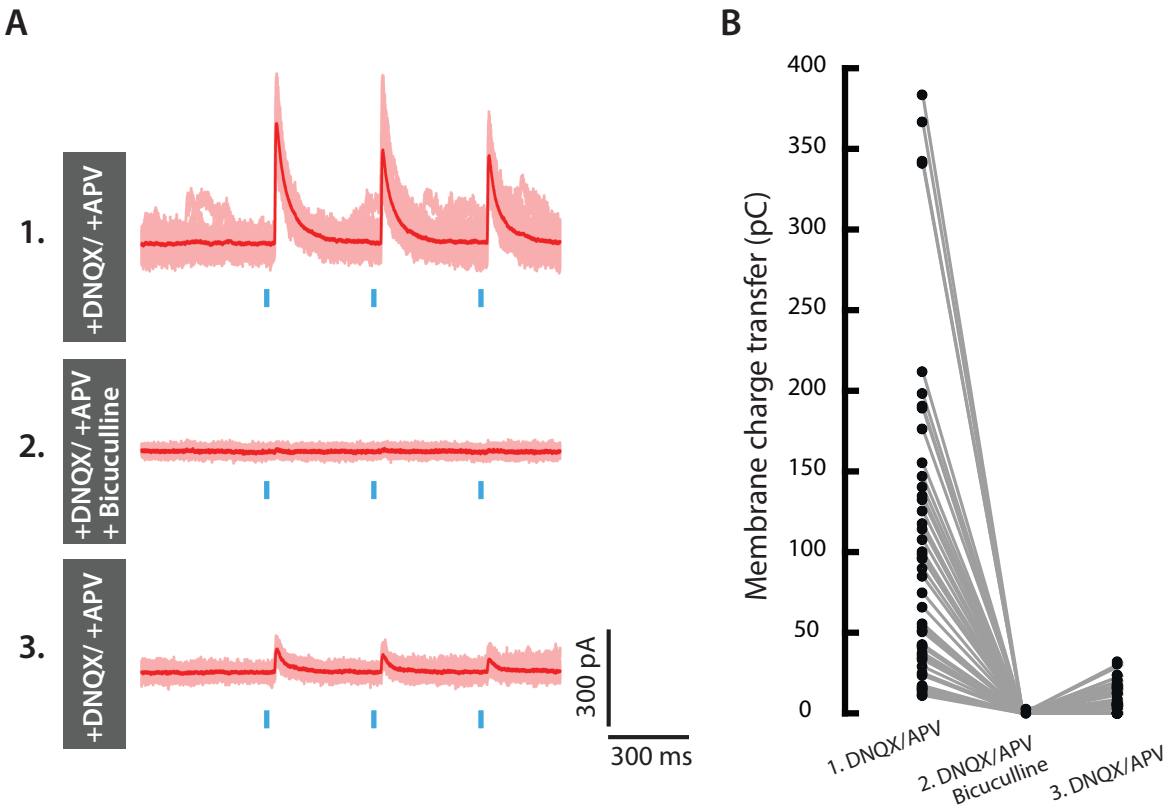

Supplementary Figure 5. Pharmacological scrutiny of laser-evoked outward inhibitory currents **(A)** Membrane current recordings of a representative PNIIA during different pharmacological treatments showing that laser-evoked IPSCs are intact in the presence of the glutamatergic synaptic blockers DNQX (10 µM) and APV (50 µM; 1. DNQX/APV), but disappear after combined exposure to DNQX/APV and bicuculline (10 µM), an antagonist of the GABAA receptor (2. DNQX/APV + bicuculline). The synaptic responses return after wash-out of bicuculline (3. DNQX/APV). **(B)** Quantification of membrane charge transfers of all neurons exposed to DNQX/APV and bicuculline. Data points are average laser-evoked responses collected from 11 neurons in 2 mice.

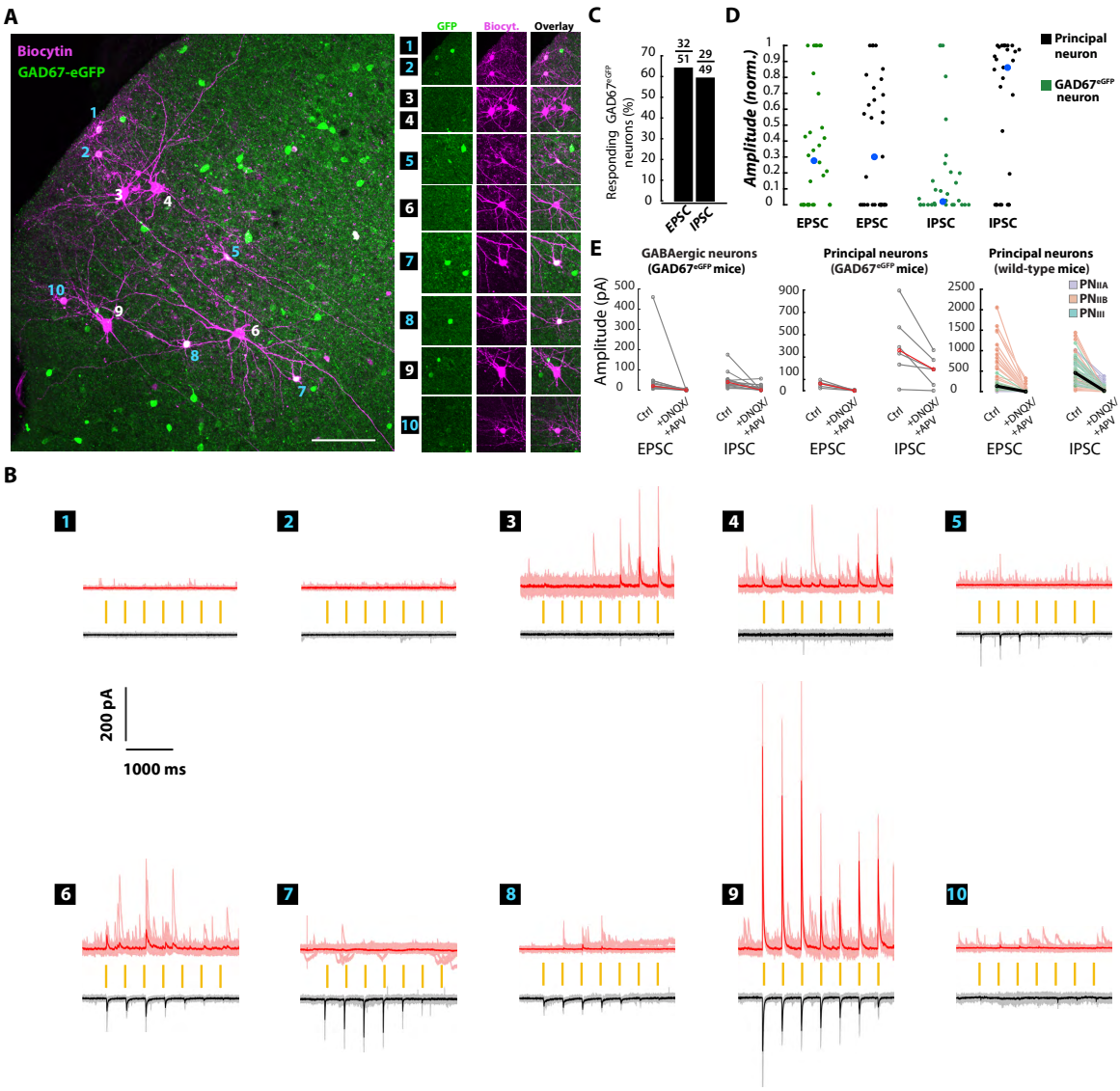

Supplementary Figure 6. Synaptic inputs from MEC to GABAergic neurons in LEC

(A) Biocytin-filled neurons (magenta) in LEC of a GAD67^{eGFP} mouse that received an injection of AAV1-hSyn-ChrimsonR-tdTomato into MEC. Recorded neurons that belong to genetically labelled GAD67^{eGFP} neurons (green) or principal neurons are indicated by blue and white numbers, respectively. Scale bar, 100 µm. **(B)** Membrane current recordings of the neurons in **A** kept at different holding potentials (black, $V_{HOLD} \approx$ -50 mV; red, $V_{HOLD} \approx$ 0 mV). Average traces (dark colors) are superimposed on the individual traces (light colors). Orange bars are laser stimuli used to active ChrimsonR^{+} MEC axons in LEC. **(C)** Percentage of recorded GAD67^{eGFP} neurons with laser-evoked IPSCs and EPSCs. **(D)** Swarm charts showing normalized amplitudes of postsynaptic currents between pairs of simultaneously recorded GAD67^{eGFP} neurons (green) and principal neurons (black) exposed to control ACSF. Blue dots are median values. **(E)** Absolute amplitudes of postsynaptic currents for GAD67^{eGFP} neurons (left) and principal neurons (middle) exposed to control ACSF and ACSF added with glutamatergic blockers (DNQX/APV) in GAD67^{eGFP} mice. For comparison, data for the same pharmacological interventions are shown for principal neurons (n = 17 PNIIA, n = 27 PNIIB, n = 21 PNIII) recorded in wild type mice (right). Median values are shown in red (left and middle diagrams) and black (right diagram).

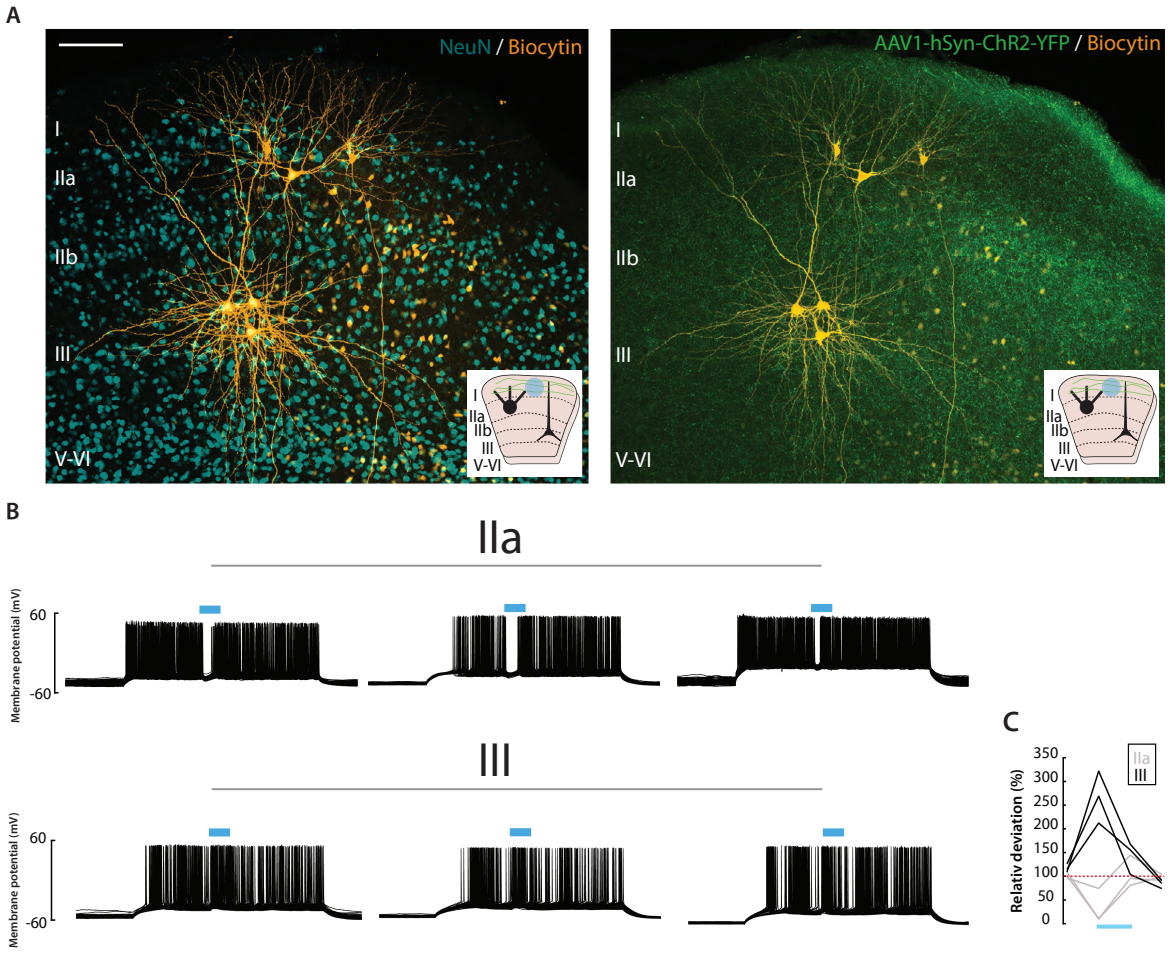

Supplementary Figure 7. Synaptic inputs from MEC give rise to different responses in principal neurons in layer IIa compared to principal neurons in layer III recorded in the same slice
(A) Six recorded and biocytin-filled principal neurons in layer IIa and layer III. The three PNIIA were recorded simultaneously, after which the three PNIII were recorded simultaneously. Voltage recordings of the neurons were carried out while medial entorhinal AAV1-hSyn-ChR2-YFP tagged axons in layer I were activated by a single 100 ms blue light pulse (insets). Scale bar, 100 µm. **(B)** Different impact of laser stimulation on the spiking activity of the recorded neurons in **A**. Note the hyperpolarizing deflections of the membrane potential during laser stimulation in the three PNIIA and the depolarizing deflections during laser stimulation in the three PNIII. Neurons were subjected to depolarizing somatic current injections to induce baseline action potential firing. **(C)** The number of action potentials fired by the neurons in **A**, **B** during laser stimulation (% relative to the number of action potentials without laser stimulation).

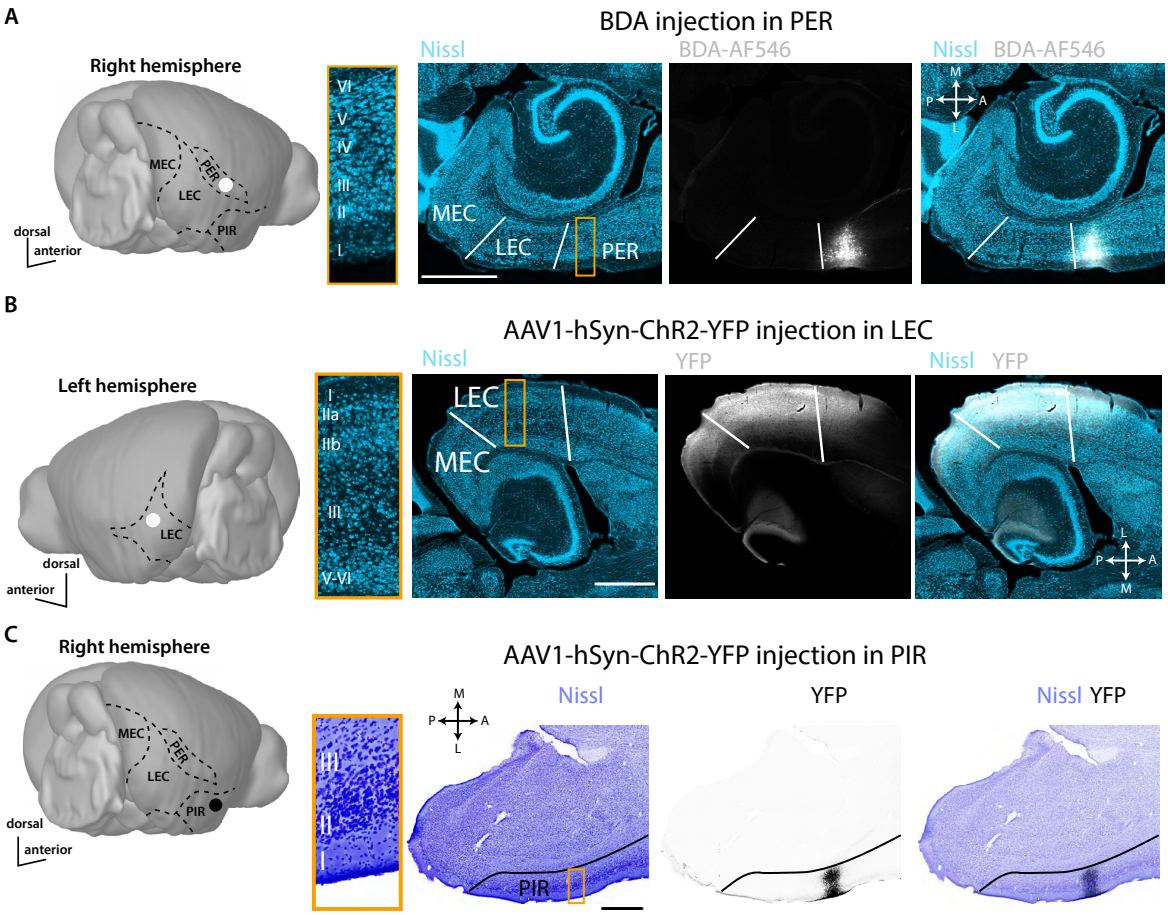

Supplementary Figure 8. Anterograde tracer injections into PER, LEC and PIR

(A) A schematic mouse brain illustrating the injection site of the anterograde tracer (BDA, white circle) in PER. A horizontal section through the ipsilateral hemisphere shows the cytoarchitecture of the hippocampal-parahippocampal region (light blue) and BDA labelling (white) in PER. Inset shows the detailed lamination pattern of PER. This case corresponds to the example shown in Fig. 4A. **(B)** Same as in (**A**), but for a virus injection into LEC. This case corresponds to the example shown in Fig. 4A. This injection also partially leaks into neighboring MEC and PER, however, this is unlikely to influence results as we have not observed a clear contralateral innervation of LEC after injections into MEC or PER. **(C)** A schematic mouse brain illustrating an injection of the anterograde virus (black circle) in PIR. A fluorescent section containing the injection site (black) is overlaid with a neighboring Nissl stained section (blue). Inset show the cytoarchitectural laminar profile of PIR. This case corresponds to the example shown in Fig. 4A. All scale bars (red) are 1000 µm. M, medial. L, lateral. A, anterior. P, posterior.

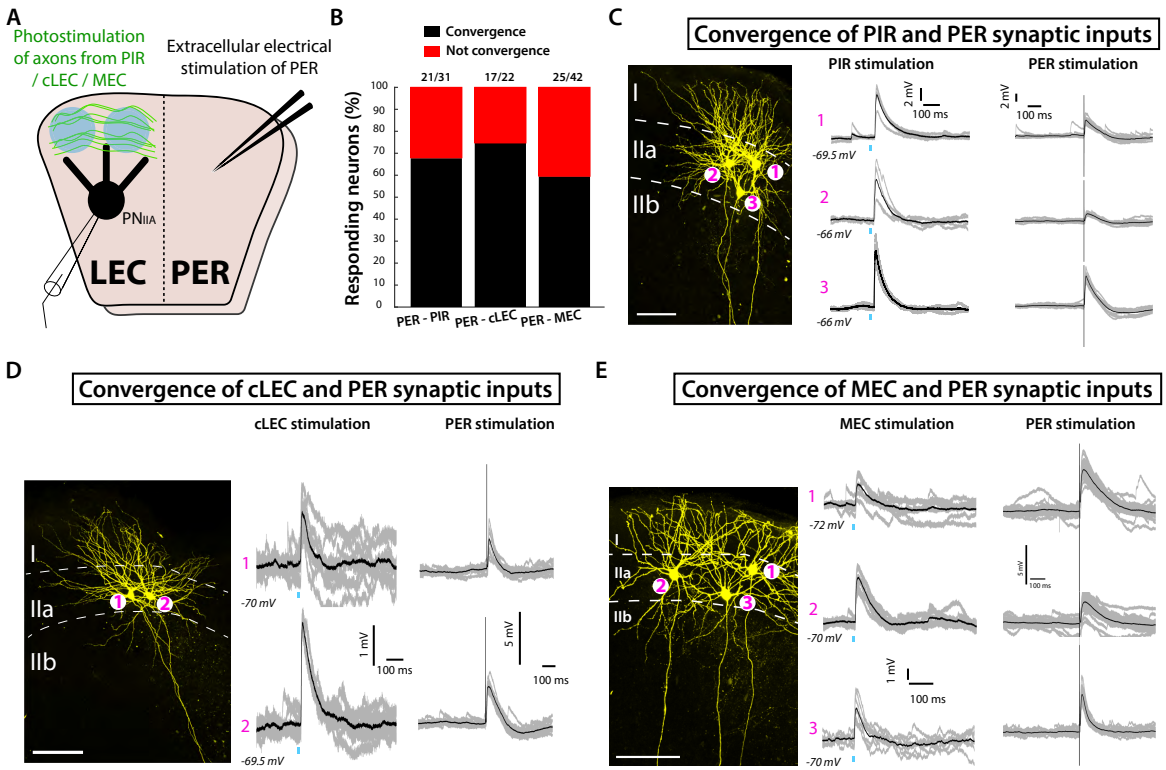

Supplementary Figure 9. Convergence of cortical inputs to principal neurons in layer IIa
(A) A schematic illustration of the experiment to combine extracellular electrical stimulation of PER with optogenetic activation of axons from either PIR, cLEC or MEC. **(B)** Bar graph showing the proportion of tested neurons that responded to stimulation of PER and either PIR, cLEC or MEC, i.e., neurons that received convergent synaptic inputs from two tested brain areas. Numbers indicate responding/tested neurons. **(C)** Electrophysiological data showing postsynaptic potentials in recorded PNIIA in response to local stimulation of PER neurons or stimulation of axons from PIR. An example cluster of biocytin-filled and recorded neurons (left) display experimentally evoked postsynaptic potentials to optogenetic activation of PIR axons locally in LEC (middle) and following electrical stimulation of neurons in PER (right). The average resting membrane potential is indicated below each voltage trace. Average membrane potential traces (black) are superimposed on traces from the individual trials (grey). Scale bar is 100 µm. **(D)** Same as in (C), but for interrogation of synaptic inputs from PER and cLEC. **(E)** Same as in (C), but for interrogation of synaptic inputs from PER and MEC.